Global ocean surface heat fluxes ~~revisited: A new dataset~~derived from the maximum entropy production framework ~~with~~accounting for ocean heat storage and Bowen ratio ~~optimizations~~adjustments

Yong Yang[1], Huaiwei Sun[1,2,3,4*], Jingfeng Wang[5], Wenxin Zhang[6], Gang Zhao[7], Weiguang Wang[8], Lei Cheng[9], Lu Chen[1], Hui Qin[1], Zhanzhang Cai[6]

[1]School of Civil and Hydraulic Engineering, Huazhong University of Science and Technology, Wuhan 430074, China

[2]Hubei Key Laboratory of Digital River Basin Science and Technology, Huazhong University of Science and Technology, Wuhan 430074, China

[3]Institute of Water Resources and Hydropower, Huazhong University of Science and Technology, Wuhan 430074, China

[4]College of Water Conservancy and Architectural Engineering, Shihezi University, Shihezi 832003, China

[5.]School of Civil and Environmental Engineering, Georgia Institute of Technology, Atlanta 30318, USA

[6.]Department of Physical Geography and Ecosystem Science, Lund University, Lund 22100, Sweden

[7.]Key Laboratory of Water Cycle and Related Land Surface Processes, Institute of Geographic Sciences and Natural Resources Research, Chinese Academy of Sciences, Beijing 100101, China

[8.]College of Hydrology and Water Resources, Hohai University, Nanjing 210098, China

[9.]State Key Laboratory of Water Resources and Hydropower Engineering Science, Wuhan University, Wuhan 430074, China

Correspondence to: Huaiwei Sun (hsun@hust.edu.cn) and Wenxin Zhang (wenxin.zhang@nateko.lu.se)

Abstract. Ocean evaporation ~~(~~, represented by latent heat flux~~,~~ (LE)~~)~~, plays a crucial role in global precipitation patterns, water cycle dynamics, and energy exchange processes. However, ~~current~~existing bulk methods for quantifying ocean evaporation are ~~subject to significant~~associated with considerable uncertainties. The Maximum Entropy Production (MEP) theory ~~offers~~provides a novel ~~approach~~framework for estimating surface heat fluxes, but its ~~effectiveness~~application over ocean surfaces ~~has not been validated.~~remains largely unvalidated. Given the substantial heat storage capacity of the deep ocean, which can create temporal mismatches between variations in heat fluxes and radiation, it is crucial to account for heat storage when estimating heat fluxes. This study ~~integrates heat storage effects and four empirical Bowen ratio formulas into the~~derived global ocean heat fluxes using the MEP theory, incorporating the effects of heat storage and adjustments to ~~improve ocean LE estimation.~~the Bowen ratio (the ratio of sensible heat to latent heat). We ~~employed~~utilized multi-source data from ~~129 globally distributed buoy stations and~~seven auxiliary turbulent flux datasets ~~for validation and comparison. We~~and 129 globally distributed buoy stations

to refine and validate the MEP model. The model was first evaluated ~~the MEP method~~ using observed data from buoy stations, ~~identifying~~and the ~~optimal~~ Bowen ratio formula ~~to enhance the model. Results indicate that accounting for heat storage~~ most effectively enhances the model performance was identified. By incorporating the heat storage effect and adjusting the Bowen ratio within the MEP model, the accuracy of the estimated heat fluxes was significantly ~~improve heat flux accuracy, with~~ improved, achieving an R^2~~=~~ of 0.99 (regression slope: 0.97) and a root mean squared error (RMSE) of 4.7 W·m^{-2} compared to observations. ~~Subsequently, we conducted a thorough evaluation of seven global turbulent flux datasets to identify the most accurate input variables (e.g., heat storage, net radiation, surface temperature) for applying the MEP method on a global ocean scale. The enhanced MEP method provided~~The improved MEP method successfully addressed the underestimation of *LE* and the overestimation of sensible heat by the original model, providing new global estimates of ~~the annual average~~ *LE* at 93 W·m^{-2} and sensible heat at 12 W·m^{-2} for the ~~period~~ annual average from 1988 to 2017. ~~Validation against observations from~~ Compared to the 129 buoy stations ~~demonstrated that,~~ the MEP-derived ~~latent heat~~global *LE* dataset achieved the highest accuracy, with a mean error (ME) of 1.3 W·m^{-2}, an RMSE of 15.9 W·m^{-2}, and a Kling-Gupta Efficiency (KGE) of 0.89, outperforming four major long-term global heat flux datasets, including J-OFURO3, ERA5, MERRA2, and OAFlux. ~~Additionally, we examined the~~ Analysis of long-term ~~spatiotemporal variability of~~ trends revealed a significant increase in global ocean evaporation~~, identifying a significant increasing trend~~ from 1988 to 2010 at a rate of 3.58 mm~~/~~ yr^{-1}, followed by a decline at ~~a rate of~~ –2.18 mm~~/~~ yr^{-1} from 2010 to 2017. ~~The current~~This dataset provides a new benchmark for the ocean surface energy budget and is expected to be a valuable resource for ~~research~~studies on global ocean warming, sea surface-atmosphere energy exchange, the water cycle, and climate change. The 0.25° monthly ~~MEP~~global ocean heat flux dataset based on the Maximum Entropy Production method (GOHF-MEP) for 1988–2017, is publicly ~~available~~accessible at ~~https://doi.org/10.6084/m9.figshare.26861767.v2~~https://doi.org/10.6084/m9.figshare.26861767.v2 (Yang et al., 2024~~,~~; last ~~access~~accessed: 28 August 2024).

1. Introduction

The ocean system plays a pivotal role in regulating the global climate by receiving and redistributing heat and freshwater, thereby influencing Earth's energy balance and the dynamics of the water cycle (Li et al., 2023; Von Schuckmann et al., 2023; Marti et al., 2022; Johnson et al., 2020). A key component ~~of~~in this ~~regulation~~system is ocean evaporation ~~(latent heat)~~, which accounts for approximately 86% of atmospheric water vapor~~and is~~, being the primary driver of the global hydrological cycle (Yu, 2011). As climate change warms the ocean, evaporation rates are ~~anticipated~~expected to rise, potentially intensifying the global hydrological cycle (Masson-Delmotte et al., 2021). This intensification could alter precipitation patterns, affecting regional water availability and freshwater ecosystems (Konapala et al., 2020; Roderick et al., 2014).

67   Therefore, precise estimation of ocean evaporation is critical to understand and quantify the global energy

68   and water budget (Iwasaki et al., 2014).

69   ~~Current~~Existing methods for calculating surface latent heat (*LE*) and sensible heat flux (*H*) ~~employ~~rely

70   on bulk transfer formulations ~~that necessitate~~, which require extensive ~~parameterization inputs,~~

71   ~~including~~input variables and parameterizations, such as temperature gradients, humidity gradients, wind

72   speed, and transfer coefficients (Fairall et al., 1996; Andreas et al., 2008). ~~Despite their widespread~~

73   ~~application~~Although widely used, these bulk methods encounter significant limitations primarily due to

74   challenges in accurately parameterizing and empirically deriving transfer coefficients (Zeng et al., 1998;

75   Robertson et al., 2020). These methods heavily depend on assumptions regarding atmospheric stability and

76   boundary layer dynamics, which may not consistently apply across diverse and complex environmental

77   conditions (Fairall et al., 2003; Andreas et al., 2013). Furthermore, uncertainties in estimating turbulent

78   transfer coefficients can lead to substantial errors in the estimation of latent heat flux. The high demands for

79   parameterization and challenges in data acquisition contribute to considerable uncertainties when

80   implementing bulk methods for calculations. While numerous energy balance-based algorithms have been

81   developed to estimate global terrestrial evapotranspiration (Wang et al., 2012; Yang et al., 2023), ~~similar~~

82   ~~efforts~~their application to ~~apply these algorithms for estimating~~ ocean surface heat flux ~~remain~~

83   ~~unexplored.~~estimation remains limited. Therefore, proposing an innovative method for estimating ocean

84   surface heat flux based on ~~rational~~ surface energy ~~allocation~~balance could yield significant theoretical and

85   practical implications. ~~This~~Such an approach ~~may~~could serve as ~~an additional reference source for~~a valuable

86   complement to existing bulk methods and their ~~derived~~associated datasets, ~~offering~~providing a ~~new~~fresh

87   methodological perspective for quantifying ~~the uncertainty of~~ ocean heat flux ~~estimation. Ultimately, this~~

88   ~~could facilitate more accurate ocean flux estimation and~~. This advancement would not only enhance ~~research~~

89   ~~on~~our ability to estimate ocean energy ~~allocation patterns.~~ fluxes with greater accuracy but also deepen our

90   understanding of their role in the global energy and water cycles.

91   The Maximum Entropy Production (MEP) model, an energy-balance-based approach, has recently

92   emerged as a novel method for simulating surface heat fluxes. Developed from Bayesian probability theory

93   and information theory, ~~it~~the MEP prioritizes the most probable partitioning of radiation fluxes (Wang &

94   Bras, 2011). The MEP model has been rigorously validated across diverse surface types and varying degrees

of surface wetness (Wang et al., 2014; Huang et al., 2017; Yang et al., 2022; Sun et al., 2022; Sun et al., 2023). Notably, the MEP model requires fewer input variables—net radiation, surface temperature, and specific humidity—yet provides accurate estimates of ~~latent heat, sensible heat~~*LE, H*, and ground heat fluxes simultaneously. Unlike bulk methods (Fairall et al., 2003), which rely on wind speed, temperature gradient, and humidity gradient, the MEP model satisfies the energy balance constraint without these dependencies. This characteristic enhances its applicability and robustness across diverse environmental conditions. However, the previous application of the MEP model over ocean surfaces has revealed significant limitations, including notable underestimations of latent heat and overestimations of ~~sensible heat flux~~*H* (Huang et al., 2017). The global multi-year averaged *LE* estimated by the MEP model ~~indicates~~indicated a value around 58 W·m^{-2}, much lower than the range of 92~109 W·m^{-2} reported by ~~other~~ remote sensing or reanalysis-based products. Conversely, MEP ~~estimates~~estimated an averaged *H* of approximately 28 W·m^{-2}, ~~which is significantly~~substantially higher ~~compared to values ranging from~~the 6 ~~to~~ 18 W·m^{-2} ~~found~~range reported in other ~~products~~studies. These discrepancies highlight substantial uncertainties in applying the MEP model to oceanic energy partitioning, highlighting the urgent need for further refinement and rigorous validation. These substantial errors in MEP-estimated oceanic fluxes may be attributed to the lack of consideration of heat storage effects. The significant impact of heat storage in deep ocean water can introduce substantial bias in estimating seasonal evaporation rates when using the Penman combination-based method (McMahon et al., 2013; Bai & Wang et al., 2023). ~~efforts~~ For instance, deep-water bodies typically store heat during the spring and release it in the fall, which can lead to overestimation of evaporation in the summer and underestimation in the fall if changes in heat storage are not accounted for (Zhao & Gao, 2019; Morton, 1994). Therefore, when estimating heat fluxes using the Bowen ratio (B_o, defined as the ratio of *H* to *LE*) energy budget-based method (including the MEP method), it is essential to incorporate heat storage effects to ensure accurate partitioning of available energy.

~~The Bowen ratio (B_o), defined as the ratio of sensible heat to latent heat flux ($B_o = H/LE$),~~ is crucial for understanding the global ocean energy partitioning process (Hicks & Hess, 1977). In the context of the energy balance-based MEP model, the significant overestimation of B_o suggests that focusing on this ratio can enhance our understanding of energy partitioning dynamics (Andreas et al., 1996). Studies have highlighted that the actual Bowen ratio over ocean surfaces (B_{oa}) often diverges from the equilibrium Bowen ratio (B_o^*)

observed under ideal conditions where the air is saturated with water vapor. The B_{oa} may deviate significantly

from B_o^* under non-equilibrium conditions, which are typical in most environments (Jo et al., 2002; Andreas

et al., 2013), posing challenges in establishing a robust relationship between B_{oa} and B_o^* (Liu & Yang, 2021).

Therefore, developing an accurate $B_o^* \sim B_{oa}$ relationship is crucial for refining the energy partitioning process

in the MEP model. The advancement of buoy observation networks has provided compelling evidence for

validating ocean heat fluxes and ~~has~~ become crucial in assessing their associated uncertainties (Bourras, 2006;

Smith et al., 2011; Bentamy et al., 2017; Liang et al., 2022~~; Tang et al.,~~).~~2023).~~ This study utilizes the energy

balance-based MEP method to estimate ocean evaporation, introducing a novel approach to redistributing

surface energy budgets and offering a streamlined parameterization scheme distinct from conventional bulk

methods used for estimating ocean heat fluxes. In contrast to existing approaches that using reanalysis-based

schemes (e.g., NCEP, ECMWF, and GEOS) and their associated parameterizations ~~(Tang et al., 2024)~~ to

estimate LE, this study employs satellite observations to directly estimate ocean heat fluxes, thereby

minimizing error propagation associated with the model structures and assimilation schemes.

Current global ocean surface heat flux datasets can be classified into five categories based on their

deriving approaches (Tang et al., 2023): remote sensing-based (e.g., J-OFURO3), atmospheric reanalysis-

based (e.g., ERA5), machine learning-based (e.g., OHFv2), in-situ based (e.g., NOC), and hybrid-based (e.g.,

OAFlux) approaches. Compared to terrestrial flux products, these ocean flux products generally have a

coarser spatial resolution ranging from 0.25° to 1.875°. Recent studies have conducted comprehensive

assessments of global ocean heat flux datasets regarding their accuracy and error characteristics across spatial

and temporal scales (Bentamy et al., 2017; Tang et al., 2023). However, substantial discrepancies remain

among these datasets, particularly in terms of spatial patterns, annual means, and interannual variabilities.

Therefore, developing a new global dataset using the innovative method could advance our understanding of

deriving algorithms, improve temporal and spatial coverage of flux variables with a higher accuracy, and

provide alternative reference to assess ocean surface heat fluxes in various applications. The primary

objectives of this study are as follows: (1) to develop and validate the MEP approach for estimating ocean

heat fluxes using observations from 129 stations; (2) to investigate the impact of heat storage on ocean energy

allocation and the influence of the Bowen ratio on energy partitioning for heat flux estimations; (3) to produce

150   a MEP-derived ocean heat fluxes product (spatial resolution: 0.25°; temporal coverage: 1988-2017) and

151   present its spatiotemporal patterns.

2. Methods

2.1 Components of ocean surface energy balance

154   The global ocean energy balance equation is as follows (Meehl, 1984; Wang et al., 2021):

$$R_n = LE + H + G \tag{1}$$

$$R_n = R_{ns} + R_{nl} = R_s^{\downarrow} - R_s^{\uparrow} + R_l^{\downarrow} - R_l^{\uparrow} \tag{2}$$

157   where R_n, R_{ns}, <u>and</u> R_{nl} are net radiation, net shortwave radiation (the difference of incoming radiation

158    $R_s^{\downarrow}$ and reflected solar radiation $R_s^{\uparrow}$), and net longwave radiation (the difference of incoming longwave

159   radiation $R_l^{\downarrow}$ and outgoing longwave radiation $R_l^{\uparrow}$) , <u>respectively;</u> H is sensible heat, LE is latent heat, and

160   G is the heat flow through the surface. Unlike terrestrial surfaces, the energy balance equation for the ocean

161   surface accounts for distinct energy exchange processes, including the impact of seawater mixing and

162   dynamics on energy transfer. For the ocean surface, the flux term G has two components,

$$G = G_t + G_v \tag{3}$$

164   where G_t is the change in the ocean heat content (ΔOHC , or heat storage), and G_v is the lateral heat

165   transported by ocean currents and other processes. The G_t can be quantified as the vertical integration of

166   temperature profile in a column of depth (Meehl ,1984, Li et al., 2023). Both the heat storage and the ocean

167   heat transport G_v are difficult to quantify, which requires large masses of hydrographic variables and

168   performing integrations at different depths. Since the ~~previous study overlooked~~<u>lateral heat transport by</u>

169   <u>ocean currents is zero at</u> the ~~calculation of evaporation on a~~ global scale (Wang et al., 2021), ~~leading to~~<u>G can</u>

170   <u>be regarded as equivalent to</u> the ~~G flux being equal to~~<u>change in ocean heat content or</u> heat storage~~.~~ <u>at the</u>

171   <u>global level.</u> For the ~~convenience in description~~<u>consistency throughout the paper</u>, this study will consider the

172   concept of G flux as equivalent to <u>the changes in the</u> heat storage.

173

2.2 The Maximum Entropy Production theory

2.2.1 The original MEP model

The MEP model ~~simulate~~simulates ocean surface heat fluxes using inputs variables of net radiation (R_n),

surface skin temperature (T_s), and surface specific humidity (q_s) under the constraint of the surface energy

balance. The latent heat, sensible heat, and surface thermal energy flux (Q) are calculated as,

$$[1 + B(\sigma) + \frac{B(\sigma)}{\sigma}\frac{I_s}{I_0}|H|^{-\frac{1}{6}}]H = R_n \tag{4}$$

$$E = B(\sigma)H \tag{5}$$

$$Q = R_{nl} - E - H \tag{6}$$

$$B(\sigma) = 6(\sqrt{1 + \frac{11}{36}\sigma} - 1), \quad \sigma = \frac{\lambda^2}{c_p R_v}\frac{q_s}{T_s^2} \tag{7}$$

$$I_0 = \rho_a c_p \sqrt{C_1 kz}(C_2\frac{kzg}{\rho_a c_p T_r})^{\frac{1}{6}} \tag{8}$$

where $B(\sigma)$ is the reciprocal Bowen ratio, σ is a dimensionless parameter that characterizes the phase

change at the ocean surface, λ (J·kg^{-1}) is the latent heat of vaporization of liquid surface, c_p (10^3 J·kg^{-1}·K^{-1})

is the specific heat of air under constant pressure, and R_v (461 J·kg^{-1}·K^{-1}) is the gas constant of water vapor.

I_0 is the "apparent thermal inertia" of air and describes the turbulent transport process of the boundary layer

based on the Monin-Obukhov similarity theory (MOST) (Wang and Bras, 2010). I_s is the thermal inertia of

the ocean surface (J·m^{-2}·K^{-1}·s$^{-1/2}$), and can be parametrized as $I_s = \sqrt{\rho c \lambda}$ (with density ρ, the specific

heat c) represents the physical property of surface ($I_s = 1.56 \times 10^3$ J·m^{-2}·K^{-1}·s$^{-1/2}$ for water surface and

1.92×10^3 J·m^{-2}·K^{-1}·s$^{-1/2}$ for ice surface) .

Over the sea ice surface, assumed to be saturated, the specific humidity q_s can be derived as a function

of surface temperature T_s using the Clausius-Clapeyron equation. (El Sharif et al., 2019; Shaman & Kohn,

2009).

$$q_s = \varepsilon \frac{e_s(T_s)}{P} = \varepsilon \frac{e_0}{P} \exp[\frac{\lambda_s}{R_v}(\frac{1}{T_0} - \frac{1}{T_s})]] \qquad (9)$$

where ε (= 0.622) represents the ratio of the molecular weight of water vapor to that of dry air, $e_s(T_s)$

denotes the saturation vapor pressure at temperature Ts, e_0 is the saturation vapor pressure at the reference

temperature T_0 (273.15 K), and P is the atmospheric pressure (mb).

2.2.2 Specific improvements on the MEP model

~~Equations (4) ~ (9) presented above represent the original formulas of the MEP model.~~ According to the

MEP theory, the net solar radiation (R_{ns}) entering the water surface medium is absorbed by the water body,

with the allocable radiation flux denoted as $R_{nl} = E + H + Q$ (Eq.6). Consequently, the expression for

ocean heat uptake (heat storage) is derived as $G = R_n - E - H = R_{ns} + Q$. While this theory has received

preliminary validation in shallower water bodies, such as lake surfaces (Wang et al., 2014), its applicability

on deeper water bodies with larger heat storage capacities in ocean surfaces requires further evaluation. This

study ~~introduces~~introduced two key hypotheses: (1) The substantial heat storage capacity of the ocean

~~can~~could exert a significant influence on seasonal latent and sensible fluxes, potentially introducing bias to

the MEP equations, (2) The notable underestimation of latent heat flux and overestimation of sensible heat

flux by the MEP model point to a significant deviation from the Bowen's ratio formula, necessitating a

reasonable correction. To address this, the study ~~proposes~~proposed two approaches for enhancing the MEP

formulas: (1) Considering the impact of heat storage in the MEP's energy balance equation, and (2) Adjusting

the theoretical equilibrium Bowen ratio within the MEP model. This can be specifically represented as

follows:

$$[1 + \frac{1}{B_o^*}]H = R_n - G \qquad (10)$$

$$B_o^* = \frac{1}{B(\sigma)} \qquad (11)$$

$$B_{oa} = a \times B_o^* + b \qquad (12)$$

where B_o^* is the equilibrium Bowen ratio, which denotes the theoretical ratio of sensible heat flux to latent

heat flux when the surface and the atmosphere are in equilibrium regarding water vapor. Correspondingly,

219   the corresponding evaporation at this condition is known as equilibrium evaporation (defined as the water

220   vapor evaporating from a saturated surface into a saturated atmosphere). To accurately predict actual

221   evaporation, a reliable functional relationship needs to be established to predict B_{oa} from $B_o{}^*$. Empirical

222   studies have introduced coefficients to correlate $B_o{}^*$ to B_{oa} under diverse environmental circumstances; for

223   instance, the Priestley–Taylor coefficient ~~is~~was expressed as (Priestley & Taylor, 1972).

224
$$B_{oa} = 0.79 \times B_o{}^* - 0.21 = \frac{0.79 - 0.21 \times B(\sigma)}{B(\sigma)} \underline{\quad\quad} \tag{13}$$

225   Further studies have led to the emergence of more updated empirical coefficients. Hicks and Hess (1977)

226   estimated the actual Bowen ratio as $B_{oa} = 0.63 \times B_o{}^* - 0.15$ by aligning it with direct observations of the

227   fluxes. Yang & Roderick (2019) deduced an empirical coefficient of 0.24 and formulated it as

228    $B_{oa} = 0.24 \times B_o{}^*$ through fitting Bowen ratio and surface temperature data across the global ocean surface.

229   Furthermore, Liu & Yang (2021) derived a new equation as $B_{oa} = 0.37 \times B_o{}^* - 0.05$ based on the

230   atmospheric boundary layer model. Given their favorable spatial applicability and representativeness, this

231   study opted to utilize these four $B_{oa} \sim B_o{}^*$ formulas to refine the MEP model and assess their suitability. The

232   revised reciprocal actual Bowen ratio ~~is~~was represented as,

233
$$\begin{cases} B(\sigma)_{a1} = \dfrac{1}{B_{oa}} = \dfrac{B(\sigma)}{0.79 - 0.21 \times B(\sigma)} \\[2mm] B(\sigma)_{a2} = \dfrac{1}{B_{oa}} = \dfrac{B(\sigma)}{0.63 - 0.15 \times B(\sigma)} \\[2mm] B(\sigma)_{a3} = \dfrac{1}{B_{oa}} = \dfrac{B(\sigma)}{0.24} \\[2mm] B(\sigma)_{a4} = \dfrac{1}{B_{oa}} = \dfrac{B(\sigma)}{0.37 - 0.05 \times B(\sigma)} \end{cases} \tag{14}$$

234   where $B(\sigma)_{a1} \sim B(\sigma)_{a4}$ represent the four empirical Bowen ratio formulas for comparisons in this study.

235   Thus, the <u>workflow of the </u>improved MEP model ~~is complemented~~<u>was conducted</u> as: replacing the original

236    $B(\sigma)$ with the corrected $B(\sigma)_a$, then combining Eq. (5), (7)-(9), and (14) into the MEP energy balance

237   equation considering heat storage (Eq. (10)), ultimately leading to the determination of latent and sensible

238   heat flux.

2.3 Input data for MEP model

The performance of both the original and improved Maximum Entropy Production (MEP) models is evaluated using observed data from in situ buoy stations, as discussed in Section 3.1. Subsequently, the optimal empirical Bowen ratio formula for the MEP model is determined through multi-site assessments. The refined MEP model is then applied to estimate global heat fluxes based on long-term remote sensing observations, detailed in Sections 3.2 and 3.3, following a comprehensive evaluation of input parameters. Specifically, the input variables of net radiation, heat storage, and sea surface temperature driving the improved MEP model are derived from the J-OFURO3 dataset, covering the period from 1988 to 2017 at a spatial resolution of 0.25° (detailed in Section 4.3).

~~2.4~~2.3 Sensitivity analysis

To quantify the influence of input variables in the MEP model on evaporation estimate at the ocean surface, the sensitivity ~~coefficients~~coefficient (S) ~~are~~was computed as (Beven, 1979; Isabelle et al., 2021),

$$S_i = \frac{\partial LE}{\partial x_i} \frac{x_i}{LE} \tag{15}$$

where S_i represents the sensitivity coefficient of LE to each variable x_i. The magnitude of S_i reflects the degree of impact of the variable's changes on LE; a larger absolute value indicates a greater influence of the variable on LE. A positive value signifies a positive correlation between evaporation and the variable's changes, while a negative value indicates a negative correlation. For example, a sensitivity coefficient of 0.5 represents that a 10% increase in the variable would result in a 5% increase in LE. The sensitivity levels can be categorized based on the absolute value |Si| (Lenhart et al., 2002; Yin et al., 2010): |Si| > 1 indicates very high sensitivity, 1 > |Si| > 0.2 denotes high sensitivity, 0.2 > |Si| > 0.05 reflects moderate sensitivity, and |Si| < 0.05 suggests negligible sensitivity.

2.~~5~~4 Data fusion methods

To ~~identify~~drive the ~~globally optimal~~ improved MEP model with high-quality input data, this study aims to obtain a heat storage ~~input data (refer to Section 4.3), this study attempts to determine whether data fusion methods could yield results superior to~~dataset with optimal accuracy. The accuracy of the heat storage dataset was assessed using three approaches: (1) individual ~~datasets. This includes~~dataset, (2) a fused dataset

generated using the Bayesian Three-Cornered Hat (BTCH) ~~Method~~method (He et al., 2020~~)~~), and ~~the Simple Arithmetic Average~~(3) an ensemble means obtained through the arithmetic average (AA) method. ~~The Three-Cornered Hat (TCH) method has been widely applied to improve~~Previous studies have demonstrated that the BTCH method effectively quantifies uncertainties across diverse datasets and improves accuracy by integrating ~~multi-source products, and it has been proven to outperform individual parent products~~multiple datasets without requiring prior knowledge (Long et al., 2017; Liu et al., 2021; Duan et al., 2024). ~~Recent evaluations of three distinct~~A recent study further evaluated various data fusion methods ~~(TCH,~~, including BTCH~~,~~ and ~~the~~ AA~~)~~ method, for addressing uncertainties in ~~consolidating~~global evapotranspiration estimates ~~have affirmed their efficacy~~derived from different datasets. The findings revealed that while both BTCH and AA are effective in ~~filtering poor~~identifying lower-quality ET ~~products, but~~datasets, their ability to ~~reliably identify superior ET products~~consistently produce higher-accuracy datasets remains uncertain and, in some cases, may even degrade the overall accuracy (Shao et al., 2022). The performance of these fusion methods is highly sensitive to the selection of input datasets. For instance, the AA method ~~may yield better results than the BTCH method in some instances~~is particularly susceptible to the influence of lower-quality datasets, especially when the sample size is small. Similarly, the performance of BTCH diminishes as the error covariance among the included datasets increases. Consequently, following a comparative analysis of the accuracy of individual, BTCH, and AA fusion ~~products~~datasets, this study ~~selects~~selected the optimal heat storage dataset to drive the MEP model. Since BTCH is not the primary focus of this study, detailed method descriptions are referred to He et al. (2020).

3. Data materials

~~3.1~~3.1 Input data for MEP model

The performance of both the original and improved Maximum Entropy Production (MEP) models was evaluated using observed data from in-situ buoy stations, as described in Section 3.2. The optimal empirical Bowen ratio formula for the MEP model was then determined through multi-site assessments. Subsequently, the improved MEP model was applied to estimate global heat fluxes using long-term remote sensing data, as detailed in Sections 3.3 and 3.4. Specifically, the input variables of net radiation, heat storage, and sea surface

291 temperature driving the improved MEP model were derived from the J-OFURO3 dataset, spanning 1988 to

292 2017 with a spatial resolution of 0.25°, as outlined in Section 4.3.

293 **3.2 In situ buoy observations**

294 A total of 129 in situ buoy sites were employed for ocean heat fluxes calculation and validation with MEP

295 model and its modified version, as listed in Table 1. About 96% of selected sites (124 of 129 all sites) ~~are~~were

296 collected from the Global Tropical Moored Buoy Array (available at https://www.pmel.noaa.gov/), which

297 consists of the TAO/TRION Pacific Ocean (69 buoys), PIRATA Atlantic Ocean (23 buoys), and RAMA

298 Indian ocean (32 buoys), and the remaining sites including Upper Ocean Processes Group (3 buoys) consists

299 of Project WHOTS - WHOI Hawaii Ocean Time-series Station (available at

300 https://uop.whoi.edu/ReferenceDataSets/whotsreference.html), Project NTAS - Northwest Tropical Atlantic

301 Station and Project STRATUS (https://uop.whoi.edu/ReferenceDataSets/ntasreference.html), and the Pacific

302 ocean climate stations (2 buoys) consists of KEO and PAPA moorings

303 (https://www.pmel.noaa.gov/ocs/data/fluxdisdel/). The availability of all buoy stations refers to the "Data

304 availability" section. The observational sites ~~cover~~covered the spatial range of 25°S~ 50.1°N latitude,

305 temporal range span from 1989/12 to 2023/12. Observational meteorological variables and heat fluxes

306 ~~includes~~included the net longwave radiation, net shortwave radiation, sea surface skin temperature, specific

307 humidity at 2m height (if available, or computed as the function of SST according to the Clausius-Clapeyron

308 equation), latent heat flux and sensible heat flux. Limited by the availability of longwave radiation

309 observations, the net radiation ~~has~~had a relatively shorter time series length compared to latent and sensible

310 heat fluxes. The surface air-sea fluxes of buoy observations ~~are~~were computed using the COARE 3.0b

311 algorithm, which have been widely applied for fluxes estimations and validations (Tang et al., 2023; Bentamy

312 et al., 2017; Fairall et al., 2003). All the selected original buoy observation (except for KEO and Papa sites)

313 records ~~are~~were in monthly temporal resolution, and the original daily observations of KEO and Papa ~~has~~had

314 been aggregated to monthly by simple average method. The spatially distributed map of all selected sites

315 ~~is~~was illustrated in Fig.S1.

316

317 **Table 1.** Information about observational ocean surface heat fluxes of 129 buoy sites

Buoy array	Buoy amount	Spatial coverage	Temporal coverage	Number of LE (H) records	Number of R_n records
TAO/TRION pacific	69	165°E-95°W 10°S-10°N	1989/12/16-2023/12/16	12377	522
PIRATA Atlantic	23	40°W-10°E, 20°S-20°N	1997/9/16-2023/12/16	2644	631
RAMA Indian	32	55°E-100°E, 25°S-15°N	2001/11/16-2023/12/16	1862	286
WHOTS	1	158°W, 22.7°N	2004/08/15-2021/08/15	205	205
NTAS	1	51°W, 15°N	2001-04/15-2020/03/15	219	219
STRATUS	1	85.4°W, 19.6°S	2000/10/15-2021/01/15	235	235
KEO	1	144.6°E, 32.3°N	2004/06/17-2023/08/12	177	177
PAPA	1	144.9°W, 50.1°N	2007/06/08-2023/11/14	181	181

318 Note: The number of records represents the effective count (excluding NA values) of latent and sensible heat
319 flux observations.

320 **3.~~2~~3 Global turbulent heat flux datasets for evaluations**

321 This study ~~evaluates~~evaluated and ~~compares~~compared 7 global turbulent heat flux products with observations,

322 categorizing them into three types: Remote sensing-based, atmosphere reanalysis-based, and hybrid-based

323 (Table 2). These seven products ~~encompass~~encompassed monthly data spanning from 1988 to 2017, with

324 spatial resolutions ranging from 0.25° to 1°. The criterion for dataset filtering ~~prioritizes~~prioritized products

325 ~~that feature~~with relatively ~~longer~~long time series, typically exceeding 15 years.

326   The Clouds and Earth's Radiant Energy Systems Synoptic Edition 4A (CERES SYN1deg_Ed4A,

327 hereafter referred to as CERES4, available at https://ceres.larc.nasa.gov/data/) offers net radiation data,

328 derived from clear-sky upward shortwave, downward shortwave flux, upward longwave, and downward

329 longwave flux measurements (Wielicki et al., 1996; Rutan et al., 2015). Another remote sensing-based

330 radiation product, the Global Energy and Water Cycle Experiment - Surface Radiation Budget (GEWEX-

331 SRB, available at https://asdc.larc.nasa.gov/project/SRB) (Pinker et al., 1992), in conjunction with CERES4,

332 ~~demonstrates~~demonstrated good accuracy in retrieving R_n, as validated by six global observing networks

333 (Liang et al., 2022).

334   The J-OFURO3 is the third-generation dataset developed by the Japanese Ocean Flux Data Sets with

335   use of the Remote-Sensing Observations (J-OFURO) research project (available at https://j-

336   ofuro.isee.nagoya-u.ac.jp/en/) (Tomita et al., 2019). It ~~calculates~~calculated turbulent heat flux with the latest

337   version of COARE3.0 algorithm, and ~~provides~~provided datasets for R_n, LE, H and SST in this study.

338   Validation with in situ observations showed that J-OFURO3 offered a superior performance of latent heat

339   compared to other 5 satellite products from 2002-2013 (Tomita et al., 2019).

340   Two Atmosphere reanalysis products including the fifth generation European Centre for Medium-Range

341   Weather Forecasts (ECMWF) atmospheric Re-Analysis52 (ERA5, available at

342   https://cds.climate.copernicus.eu/cdsapp#!/dataset/reanalysis-era5-single-levels-monthly-

343   means?tab=overview) (Hersbach et al., 2020), and the Modern-Era Retrospective analysis for Research and

344   Applications Version2 (MERRA2, available at

345   https://disc.gsfc.nasa.gov/datasets/M2TMNXOCN_5.12.4/summary) (Gelaro et al., 2017). Both ERA5 and

346   MERRA2 products ~~employ~~employed the bulk formula based on the MOST to calculate heat fluxes.

347   Validation results from previous studies have demonstrated good consistency with buoy estimates regarding

348   heat fluxes (Pokhrel et al., 2020; Chen et al., 2020).

349   The OAFlux (available at https://oaflux.whoi.edu/), a hybrid-based product developed under the

350   Objectively Analyzed Air-Sea Fluxes (OAFlux) project at the Woods Hole Oceanographic Institution (WHOI)

351   (Yu et al., 2008), was utilized for comparisons with ocean heat fluxes derived from distinct methods. This

352   product calculates fluxes based on the COARE3.0 bulk algorithm and employs a variational objective

353   analysis to determine the optimal fitting of independent variables. Detailed descriptions on all utilized global

354   turbulent heat fluxes products, and their validation performances against buoy observations with reported

355   studies ~~are~~were available in Tang et al (2023).

356

357   **Table 2.** The information of the 7 used global radiation and heat fluxes products

Product	Variables	Spatial resolution	Time span	Type	Reference
CERES4	R_n	1°	2000-2017	Remote sensing	Rutan et al. (2015)
GEWEX-SRB	R_n	1°	1988-2017	Remote sensing	Pinker et al. (1992)

J-OFURO3	R_n, SST, LE, H	0.25°	1988-2017	Remote sensing	Tomita et al. (2019)
ERA5	R_n, LE, H, P	0.25°	1988-2017	Atmosphere reanalysis	Hersbach. et al. (2020)
MERRA2	R_n, LE, H	$1/2° \times 2/3°$	1988-2017	Atmosphere reanalysis	Gelaro et al. (2017)
OAFlux	LE, H	1°	1988-2017	Hybrid-based	Yu et al. (2008)
IAPv4-OHC	OHC	1°	1988-2017	Hybrid-based	Cheng et al. (2017)

358

359

360

3.~~3~~4 Ocean heat content data

Remote sensing data for heat storage (G) was primarily ~~derive~~derived from two categories: ~~one is~~the first category included data obtained from the residual of the energy balance equation (R_n-LE-H), including J-OFURO3, ERA5, and MERRA2; the ~~other is~~second category was calculated ~~as~~from changes in Ocean Heat Content (OHC). The ocean heat content data ~~is~~was obtained from IAP OHC gridded analysis (IAPv4, available at http://www.ocean.iap.ac.cn/) dataset, covering ocean depth of 0-6000m (Cheng et al., 2017), and has been extensively utilized in global ocean heat analysis, ocean warming, and climate change studies (Li et al., 2023; Cheng et al., 2022; Cheng et al., 2024). The delta OHC ~~is~~was calculated using the numerical differentiation method (Xu et al., 2019) as $\Delta\mathrm{OHC(i)} = \dfrac{OHC(i+1) - OHC(i-1)}{2\Delta i}$, i denotes the OHC of i-th month. At the WHOTS site, this study compared the OHC changes at different depths with the observed G ~~(,~~ derived as Rn-LE-H~~) (Fig.~~ (Table S1). Since the OHC variation from 0~100m depth ~~exhibits~~exhibited the smallest error with the observations, the data from 0~100m depth range were chosen as the heat storage. This study ~~assesses~~assessed the suitability of G flux and $\Delta\mathrm{OHC}$ for global evaporation estimations, with the aim of minimizing the errors introduced by input variable data in the MEP model.

This study ~~evaluates~~evaluated the accuracy of all the variables R_n, T_s, and G using the aforementioned datasets on a global scale by comparing them against buoy observations (in Section 4.3), to optimize input accuracy for driving the MEP model. To maintain consistency in the analysis, this study ~~resamples~~resampled all products to ~~a~~ 1° spatial resolution when comparing the Bowen ratio across multiple products. Nevertheless, when conducting site validations with buoy observations, the original resolution of the data ~~is~~was preserved to minimize uncertainty attributable to scale effects.

4. Results

4.1 The new MEP model with heat storage and the revised Bowen ratio formulas

To demonstrate how the MEP model has been developed and improved, we ~~show~~showed the comparisons of different MEP models in simulating heat fluxes across 129 global buoy stations (Fig.1). Limited by the availability of R_{nL} data, we used $LE + H$ instead of the available energy ($R_n - G$), enabling the utilization of more observational records to verify the MEP model. The original MEP model (without considering heat

storage) ~~shows~~showed a significant negative correlation between *LE* and *H* (with R^2 ~~exceeds~~exceeding 0.65

as in Fig.1a & Fig.1c), with considerable errors, where the RMSE of *LE* ~~is~~was 134.6 W·m^{-2} and that of *H*

~~is~~was 37 W·m^{-2}. ~~Upon modification by considering~~After incorporating the influence of heat storage effects

(~~Represented~~represented as *MEP_M*, as depicted in Fig.1b ~~&~~and Fig.1h), the MEP-simulated *LE*

~~shows~~showed a good consistency ~~(R² = 0.97)~~ with ~~the~~ buoy observations, ~~but an approximate 25%~~

~~underestimation (slope = 0.75) was observed,~~ with ~~RMSE~~an R^2 value of 0.97 and a reduced ~~to~~RMSE of 27

W·m^{-2}. However, ~~it reveals an overall underestimation (approximate 25%)~~the *MEP_M* method revealed a

significant bias in the partitioning of *LE* and ~~a large overestimation of~~ *H*~~.~~ from the available energy.

Specifically, *LE* was underestimated by 25% (regression slope = 0.75), while H was overestimated by 46%

compared to observations. This finding ~~agrees~~agreed with previous research findings that equilibrium

evaporation ~~tends~~tended to underestimate actual evaporation from saturated surfaces by 20%~30% (Yang &

Roderick, 2019; Philip, 1987). The ~~physical significance of this phenomenon can be explained~~significant

difference between B_{oa} and B_{o*} could exist as the equilibrium evaporation ~~being~~is considered as the lower

limit of actual evaporation from saturated surfaces~~, causing~~ typically falls below the actual evaporation

(Priestley and Taylor, 1972). To address the deviation between B_{oa} and B_o^*, it is necessary to convert the

equilibrium Bowen ratio into the actual Bowen ratio, allowing for a more reasonable and accurate allocation

of surface energy budget.

After ~~modifying MEP's energy allocation using~~incorporating the effects of heat storage, four variants

of the MEP model were developed by replacing B_{o*} with B_{oa} derived from four different empirical ~~Bowen~~

~~ratio~~formulas ~~(denoted~~. These variants were defined as follows: *M_0.24*~~,~~ (where $B_{oa}=0.24 B_o^*$), *M_0.79*~~,~~

(where $B_{oa}=0.79 B_o^*-0.21$), *M_0.63*~~,~~ (where $B_{oa}=0.63B_o^*-0.15$), and *M_0.37*~~), the accuracy of MEP predated~~

~~latent and sensible heat have been~~ (where $B_{oa}=0.37B_o^*-0.05$). Adjusting the Bowen ratio significantly

improved~~.~~ the accuracy of the energy flux estimates. The ~~MEP~~ simulated *LE* exhibited strong agreement with

observations, with all R^2 exceeding 0.97 and RMSE ranging from 4.7 W·m^{-2} (for *M_0.24*) to 7.1 W·m^{-2} (for

M_0.79), which ~~is~~was lower than that derived from ~~equilibrium Bowen ratios~~B_o^* (RMSE = 27 W·m^{-2}). Both

M_0.79 and *M_0.63* tended to underestimate *LE*, especially when *LE* exceeded 200 W·m^{-2} (Fig. 1d and

Fig.1e). ~~The results for sensible heat flux simulated by MEP were similar to those for *LE*~~For the simulated

H, the *M_0.24* outperformed the other three, showing the smallest errors and highest R^2.
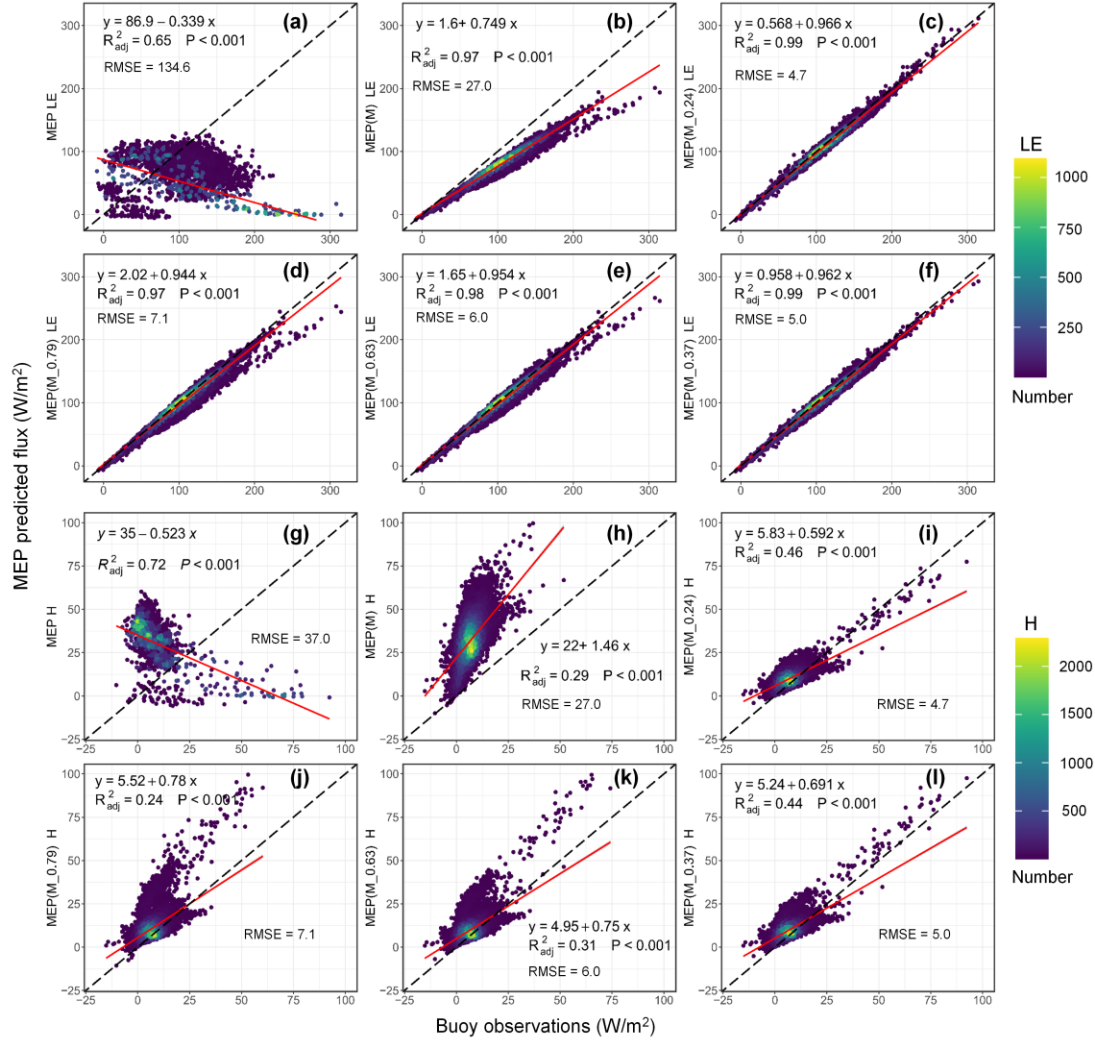
415

416

Figure 1. Scatter density plots of monthly latent heat flux (a~f) and sensible heat flux (g~l) derived by the original and modified MEP methods versus observations from 129 buoy stations (as in Table 1). (a) The original MEP method, (b) The modified MEP method considering the heat storage effect, (c) The modified MEP method considering both the heat storage and empirical Bowen ratio formula $B_{oa}=0.24B_o^*$, (d)~(f) for the modified MEP method considering both the heat storage and empirical Bowen ratio formulas $B_{oa}=0.79B_o^*-0.21$, $B_{oa}=0.63B_o^*-0.15$, and $B_{oa}=0.37B_o^*-0.05$. (g)~(l) are the same with (a)~(f) but for sensible heat flux.

424

Specifically, the spatial ~~patterns of simulated~~ errors for the four ~~modified~~variants of the MEP ~~formulas~~model were obtained (Fig. 2), ~~as well as~~along with the ~~prediction~~ errors across ~~various~~different observational buoy arrays (Fig. 3). Overall, the four ~~modified~~variants of the improved MEP ~~formulas exhibit~~ models demonstrated relatively lower ~~errors~~bias at low latitudes (10°S~ to 10°N~,~) but ~~they demonstrate~~ exhibit larger ~~discrepancies at~~bias in higher ~~latitudes, especially for~~latitude regions (above 15°N), particularly

18

430 at the KEO, WHOTS, and STRATUS buoy sites. Comparing the four formulas across varying latitudes, the

431 *M_0.24* formula ~~exhibits~~exhibited the smallest RMSE (ranging from 3.6 to 12 W·m^{-2}) (Fig. 3c), while the

432 *M_0.79* formula ~~shows~~showed the largest errors (RMSE ranging from 3.9 to 26.6 W·m^{-2}). This consistency

433 ~~is~~was also evident in the Kling-Gupta Efficiency (KGE) coefficient, with *M_0.24* demonstrating superior

434 performance in terms of accuracy, robustness, and adaptability. In term of *M_0.24* formula, the prediction

435 errors across observational arrays ranked as follows: RAMA < PIRATA < TAO/TRION < PaPa < KEO <

436 STRATUS < WHOTS < NTAS. The arrays with relatively larger RMSE (NTAS in the Atlantic Ocean,

437 WHOTS, and STRATUS in the Pacific Ocean) may originate from the larger observed values of LE (Fig.
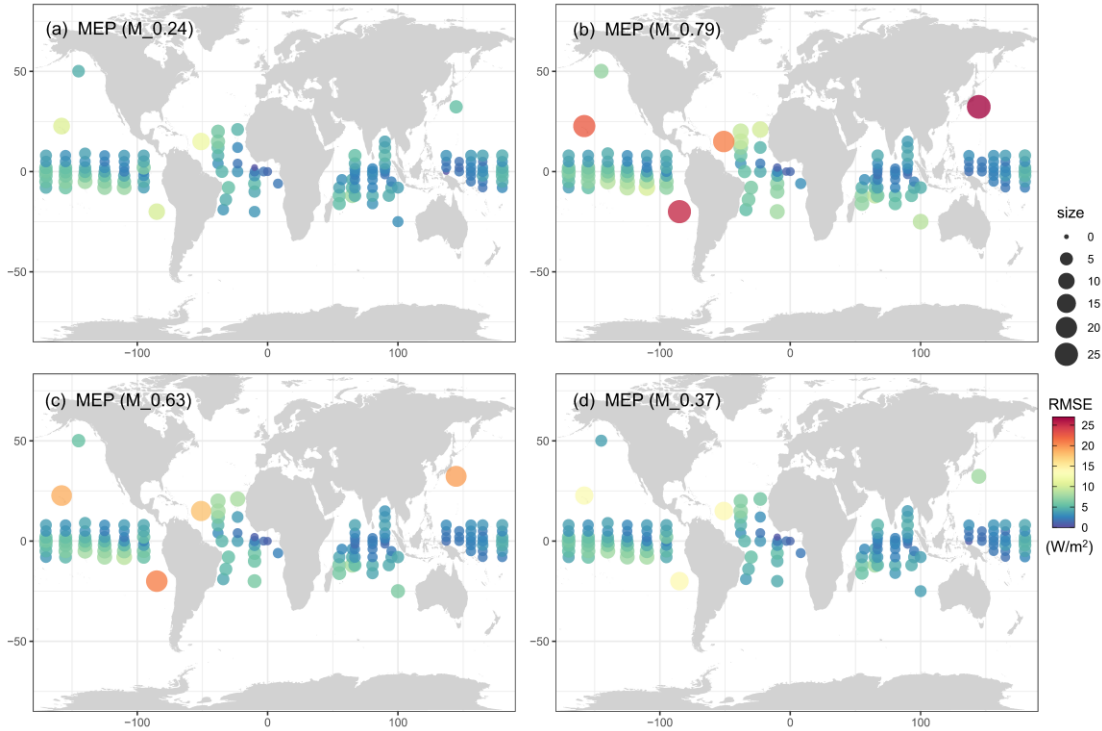
438 S2).

439

440
441 **Figure 2.** Spatial distribution of RMSE values in the comparison ~~of~~between latent heat flux estimated by
442 the improved MEP method (modified by four different Bowen ratio formulas) ~~with~~and buoy observations
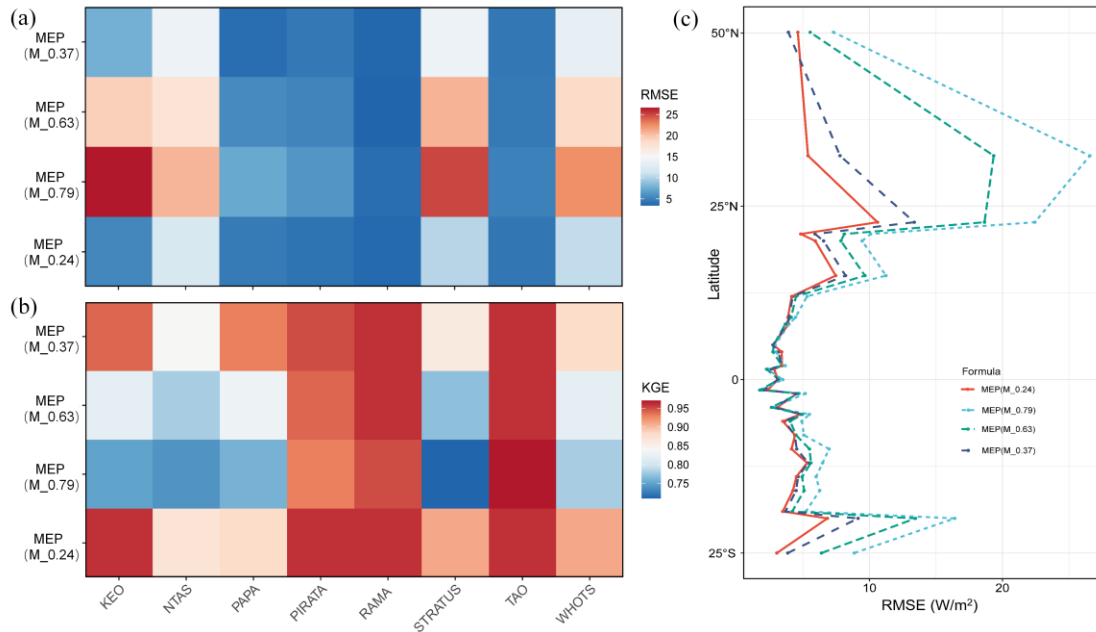443 from 129 stations.
444

Figure 3. Comparisons ~~of~~between latent heat flux estimated by the improved MEP method ~~with~~using four empirical Bowen ratio formulas and the buoy observations from each buoy array in term of RMSE (a) KGE value (b), and latitudinal means of RMSE ~~of four empirical Bowen ratio formulas (c).~~(c). Latitudinal means are based on data from 129 available buoy sites.

4.2 Dynamics of heat fluxes and Bowen ratio between original and improved MEP model

To thoroughly investigate the role of heat storage in the partitioning of surface energy and its implications for the temporal dynamics of heat fluxes, we selected the KEO site for detailed analysis. This ~~decision~~selection was based on the site's ~~extensive~~ long-term observational records and notable variability in flux patterns, which ~~offer~~offered an ideal context for a rigorous comparison of model-simulated error margins.

   The improved MEP methods demonstrated comparable performance in estimating heat fluxes at the KEO site when compared with ~~128~~ other 128 sites (Fig. S3, Fig. 1), with the MEP (M_0.24) model exhibited the most effective performance. Analysis of the time series data revealed significant variations in latent heat, sensible heat, and Bowen ratio (Fig. 4). In the original MEP theory, the estimated *LE* ~~exhibits~~exhibited an opposite variation cycle (peak versus trough) compared to the observations. For instance, over a yearly period, the observed peak in *LE* occurred in January 2005 (269 W·m^{-2}) and the trough in June 2005 (6.9 W·m^{-2}). In contrast, the MEP simulated the peak in *LE* to occur in August 2005 (105 W·m^{-2}) and the trough in December 2004 (0.7 W·m^{-2}), resulting in a phase difference of 7 months for the peak and 6 months for the trough values.

20

465   Sensible heat flux (Fig. 4b) showed similar phase differences: observed H peaked in January 2005 (79 W·m⁻

466   ²) and reached its minimum in June 2005 (-3 W·m⁻²), whereas MEP simulated H to peak in August 2005 (46

467   W·m⁻²) and reach its minimum in December 2004 (0.6 W·m⁻²), consistent with the pattern observed for LE.

468   It ~~is~~was noteworthy that the original MEP model simulated variations in LE and H align with R_n (Fig. S4),

469   which ~~is~~was reasonable over land where the small G value can often be disregarded. However, over the ocean,

470   the observed variations in R_n and LE do not align in terms of their cycles. The maximum R_n occurred in June

471   2004 (329 W·m⁻²) and the minimum occurred in December 2004 (142 W·m⁻²), with a 6-month delay in

472   relation to the variations in LE. Specifically, the peak R_n corresponded to the trough of LE, and the trough R_n

473   corresponded to the peak of LE. This delay ~~indicates~~indicated that the heat storage effect ~~delays~~delayed the

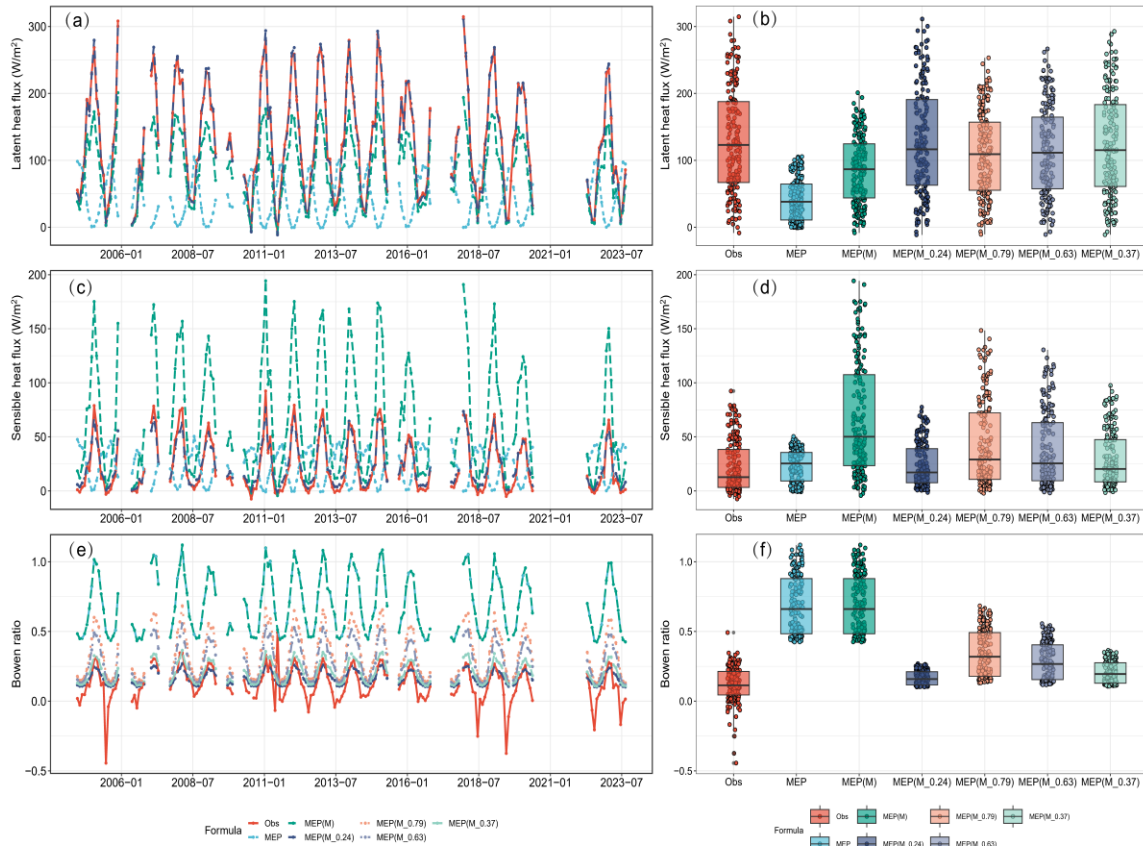474   peak of LE and ~~alters~~altered the seasonal variations of LE and H.

475

476

Figure 4. ~~MEP model predicted~~The inter-annual variations (a, c and e) and variabilities (b, d, and f) for latent heat flux ~~(a),~~, sensible heat flux ~~(c),~~ and Bowen ratio ~~(e) versus observations, and corresponding boxplots~~ ~~(b, d, f) of these variables~~ at KEO site from June 17, 2004, to August 12, 2023. The fluxes in the comparison include observations and the estimates from MEP using the original formula (MEP), the formula incorporating the ocean heat storage (MEP(M)), and four other formula considering both ocean heat storage

482 and adjustment of Bowen ratio. Note that the (a) and (c) only display results using MEP *(M_0.24)* among all
483 four empirical Bowen ratio formulas for clearer comparison.
484

485   For the ~~variation pattern~~patterns of the Bowen ratio, both the original MEP formula and the modified

486 formulas ~~exhibit~~exhibited consistent patterns with the observed values. The observed maximum Bowen ratio

487 occurred in January 2005 (0.29~~),~~) and the minimum in June 2005 (-0.4). However, the original MEP formula

488 simulated a maximum of 1.01 and a minimum of 0.44, indicating a significant overestimation compared to

489 the observed Bowen ratio. This discrepancy ~~suggests~~suggested that on the ocean surface, the available energy

490 (R_n-G) ~~is~~was predominantly allocated to *LE* (Fig.S4). Among the four empirical formulas, *M_0.24* simulated

491 *LE*, *H*, and Bowen ratio values were closest to the observed values. The median of the observed Bowen ratio

492 was 0.11, while the original MEP Bowen ratio was 0.66. Among the four modified Bowen ratio formulas

493 (*M_0.24*, *M_0.79*, *M_0.63*, *M_0.37*), their median Bowen ratios were 0.15, 0.32, 0.27, and 0.19 respectively,

494 with *M_0.24* being the closest to the observed Bowen ratio.

495   Heat storage is crucial for the energy distribution process over the ocean surface. While the original

496 MEP formulas have been effectively validated when applied to surfaces with shallow depths such as water

497 and snow (Wang et al., 2014), they exhibit significant uncertainty when applied to the ocean surface. This

498 discrepancy primarily arises from the fact that land is a non-transparent medium with relatively small heat

499 storage values at monthly scales. Similarly, shallow water bodies also exhibit small heat storage values that

500 can often be ignored. In the study by Wang et al. (2014), for example, two lakes with depths of 2m (Lake

501 Tämnaren) and 4m (Lake Råksjö) still resulted in underestimated *LE*. However, for deeper lakes (generally >

502 3m depth), heat storage becomes significant and cannot be neglected (Zhao et al., 2016; Zhao & Gao, 2019).

503 On deep ocean surfaces, with the most recent average depth estimate of 3,~~682 meters~~682m from NOAA

504 satellite measurements, heat storage variations can influence depths up to 6,~~000 meters~~000m (Cheng et al.,

505 2017). Therefore, the impact of heat storage ~~is~~was substantial and cannot be disregarded. In the original MEP

506 theory, heat storage was not considered in the energy balance equation, where it was assumed that the net

507 solar radiation (R_{ns}) is absorbed by the ocean and R_{nL}= LE + H + Q. Then, the heat storage was obtained as

508 $G = R_{ns} + Q$. In this study, we compared the characteristics of MEP-derived G ($R_{ns} + Q$) with the observed *G*

509 flux ($G = R_n - LE - H$ (Fig. S5). MEP-derived *G* ~~shows~~showed a good correlation ($R = 0.96$) and consistent

510 trends with the observed values (Fig. S5a & b), ranging from -4 to 81 W·m^{-2}. However, MEP-calculated *Q*

(ranged from -210 to -65 W·m^{-2}) ~~exhibits~~exhibited a negative correlation with the observed G (which ranged

from -386 to 200 W·m^{-2}). Both MEP-derived G and Q fluxes ~~are~~were significantly underestimated. Therefore,

the prediction errors in LE and H ~~originates~~originated from the inability to accurately quantify the heat

storage. Hence, considering the influence of heat storage ~~is~~was crucial for accurately predicting LE and H

over the ocean surface.

4.3 Evaluation of global radiation and heat storage flux

4.3.1 Evaluation of net radiation

After considering the effect of heat storage and the Bowen ratio, the improved MEP method demonstrated

its high performance at the site scale. The results ~~suggest~~suggested that improved MEP method ~~holds~~held

substantial promise for further application at a global scale. To facilitate this, we assessed the primary input

variables of the improved MEP method (including R_n, G, and T_s) to identify datasets with the best accuracy.

Net radiation, as the primary variable in the energy balance equation, significantly ~~influences~~influenced

the uncertainty of the MEP model (Huang et al., 2017). Selecting a reliable R_n product ~~is~~was essential for

accurately estimating global latent and sensible heat fluxes. Previous studies have evaluated the available

global ocean surface R_n datasets at daily scales using observations from 68 moored buoy sites (Liang et al.,

2022). In this study, we conducted a comprehensive evaluation of current ~~mainstream~~available monthly R_n

products, including three remote sensing-based products (~~CERES~~CERES4, GEWEX-SRB, and JOFURO3)

and two atmosphere reanalysis-based products (ERA5 and MERRA2~~).~~) at 129 buoy sites. All products

exhibited good consistency with buoy observations (Table 3 and Fig. S6), with R^2 values greater than 0.78.

In terms of RMSE, the error rankings for all products were as: J-OFURO3 (10 W·m^{-2}) < ERA5 (39.03 W·m^{-2}

) < ~~CERES~~CERES4 (40.67 W·m^{-2}) < GEWEX-SRB (41.83 W·m^{-2}) < MERRA2 (49.23 W·m^{-2}). It ~~is~~was

evident that J-OFURO3 demonstrated the highest accuracy, as indicated by RMSE, NSE, and KGE statistics.

This ~~study is~~result was also consistent with previous assessments of global ~~radiation~~R_n (Liang et al., 2022),

emphasizing J-OFURO3 as the least erroneous among all individual products and superior to existing

alternatives including CERES4, ERA5, MERRA2, GEWEX-SRB, JRA55, OAFlux, and TropFlux.

Table 3. Evaluation of global monthly net radiation products against buoy observations

Products	R^2	ME (W·m^{-2})	MAE (W·m^{-2})	RMSE (W·m^{-2})	PBIAS (%)	NSE	KGE
J-OFURO3	**0.96**	**1.6**	**7.3**	**10.0**	**1.0**	**0.96**	**0.97**

ERA5	0.79	28.8	30.3	39.0	17.8	0.45	0.77
MERRA2	0.78	39.7	41.2	49.2	24.8	0.15	0.68
~~CERES~~CERES4	0.81	31.4	32.6	40.6	19.6	0.42	0.76
GEWEX-SRB	0.78	32.6	33.8	41.8	20.2	0.37	0.76

Note: The evaluation period for all datasets is 1988-2017, except for ~~CERES~~CERES4, which spans from March 2000 to December 2017. The best-performed statistics are indicated in bold type.

4.3.2 Evaluation of heat storage

The study ~~underscores~~underscored the importance of considering heat storage in simulating heat fluxes using the improved MEP model. For the first time, we assessed global heat storage using the J-OFURO3, ERA5, MERRA2, and ΔOHC datasets. In addition to assessing these individual datasets, we investigated the potential for enhancing accuracy through data fusion methods. We employed the BTCH and AA method to fuse heat storage data and compared the accuracy between individual datasets and fused datasets (Table 4). The results ~~reveal~~revealed that while using the AA method (e.g., AA4) to fuse yields smaller errors compared to ERA5, MERRA2, and ΔOHC, it still failed to achieve the accuracy of the J-OFURO3 product. Similarly, the BTCH method, despite fusing data from three or four sources, also does not match the accuracy of the J-OFURO3 method, as indicated by metrics of R^2, RMSE, and KGE. The heat storage derived from J-OFURO3 data ~~shows~~showed high consistency with observations (R^2=0.95), as illustrated in Fig. 5 (spatial distribution of errors depicted in Fig.S7). Therefore, this study ~~adopts~~employed the heat storage data derived from the J-OFURO3 dataset as the input for the MEP model.

To ensure consistency with radiation data source, the Sea ~~surface temperature~~Surface Temperature (*SST*) data from J-OFURO3 ~~is~~was utilized for T_s inputs, which ~~is~~was derived as the ensemble median from 12 global *SST* products (Tomita et al., 2019). Ultimately, the input variables including net radiation, heat storage, and sea surface temperature for driving MEP model ~~are~~were all determined from the J-OFURO3 dataset spanning from 1988 to 2017. Saturated specific humidity ~~is~~was computed as a function of *SST* and surface air pressure (from ERA5) using the Clausius‑Clapeyron equation. The reliability of gridded data for the variables R_n, G, and T_s ~~are~~were simultaneously examined at an observational site (Fig.S8), where all three variables demonstrated high consistency with observed data from August 2004 to December 2017 (with R^2 > 0.96), effectively capturing the monthly dynamics of R_n, G, and T_s.

Table 4. Assessment of monthly heat storage between global remote sensing datasets and buoy observations

Products	R^2	ME (W·m⁻²)	MAE (W·m⁻²)	RMSE (W·m⁻²)	PBIAS (%)	NSE	KGE
J-OFURO3	**0.95**	**-3.5**	**15.3**	**19.7**	**-7.4**	**0.94**	**0.91**
ERA5	0.88	7.0	25.1	33.2	14.8	0.84	0.80
MERRA2	0.86	11.6	27.1	36.1	24.5	0.81	0.72
OHC	0.35	-48.2	64.4	86.9	-101.9	-0.11	-0.10
BTCH3-1 (E M J)	0.89	7.1	22.8	30.5	15.1	0.86	0.81
BTCH3-2 (E M O)	0.88	4.6	24.0	31.4	9.9	0.85	0.86
BTCH4	0.91	5.9	19.7	26.2	12.5	0.90	0.86
AA2(EM)	0.87	9.3	25.4	34.1	19.7	0.83	0.76
AA3 (EMJ)	0.91	4.7	20.2	26.7	10.1	0.90	0.87
AA4 (E M J O)	0.91	11.5	21.4	28.6	24.4	0.88	0.74

Note: BTCH3-1 represents the fusion of three products (ERA5, MERRA2, and J-OFURO3) using the BTCH method; TCH3-2 represents the fusion of ERA5, MERRA2, and OHC; BTCH4 represents the fusion of ERA5, J-OFURO3, MERRA, and OHC. AA denotes the Simple Arithmetic Average (AA) method. The evaluation period spans from 1988 to 2017, and the best-performed statistics are indicated in bold type.
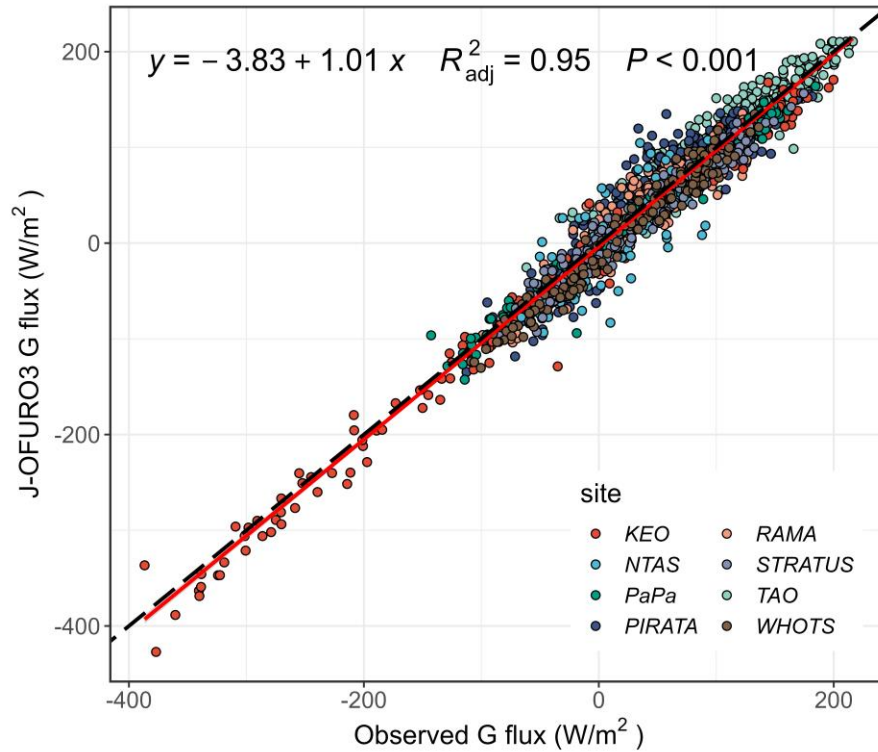

Figure 5. Assessment of heat storage (G) flux derived from remote sensed J-OFURO3 dataset against buoy observations. Distinct colors represent data collected from different buoy arrays.

4.4 Estimating long-term global ocean surface heat fluxes by improved MEP model

574 4.4.1 New estimate of global latent and sensible heat fluxes

575 After identifying the optimal driving dataset, this study ~~employs~~employed the best-performed improved MEP

576 method (i, e., *M_0.24*, hereinafter referred to as MEP for simplicity, while the original MEP formula ~~is~~was

577 denoted as *MEP (ori*~~)~~)*)* for global scale estimation, producing new estimations of latent and sensible heat

578 fluxes for the period 1988-2017 (Table 5). The MEP model calculated the multi-year average *LE* as 92.87

579 $W\cdot m^{-2}$ and the sensible heat flux as 12.27 $W\cdot m^{-2}$ from 1988 to 2017. In comparison, *LE* ~~ranges~~ranged from

580 88.95 (OAFlux) to 100.54 $W\cdot m^{-2}$ (MERRA2), and *H* ~~ranges~~ranged from 10.17 (J-OFURO3) to 13.16 $W\cdot m^{-}$

581 ^{2} (MERRA2) for the other four products. The original MEP method yielded estimates of *LE* as 52.70 $W\cdot m^{-2}$

582 and *H* as 25.07 $W\cdot m^{-2}$, significantly underestimating *LE* and overestimating *H* compared to estimates from

583 other products. As previously demonstrated (Sections 4.1 & 4.2), the original MEP method overestimated *G*

584 (42.20 $W\cdot m^{-2}$) and exhibited notable deviations in the Bowen ratio. Therefore, the improved MEP method

585 ~~provides~~provided a more reasonable global estimation of *LE* and *H*.

586 Regarding the global spatial pattern (Fig.6), the MEP-derived latent heat ~~shows~~exhibited higher values

587 in low-latitude regions but ~~notably decreases~~significantly decreased beyond 45° latitude. The highest *LE*

588 values ~~are~~were observed in the southern Indian Ocean near Australia, the Pacific and Atlantic regions near

589 South America, and the Indian Ocean near southern Africa. The peak values ~~are~~were observed within western

590 boundary current systems (~~ranging~~ranged from 200 to 260 $W\cdot m^{-2}$), including the Gulf Stream in the North

591 Atlantic and the Kuroshio in the western North Pacific. Impacted by the variations in oceanic currents near

592 the equator, two general areas of higher *LE* have emerged (Yu et al., 2011), leading to notably low *LE* at the

593 equator (88 $W\cdot m^{-2}$), peaking at ~18°S at 132 $W\cdot m^{-2}$ (Fig. 6 & Fig._7). The MEP estimated *LE*

594 ~~exhibits~~exhibited a similar spatial pattern with other four products globally (Fig.6), particularly resembling

595 OAFlux between 15°S and 15°N (Fig. 7). Overall, for the region between 30°S and 30°N, the ~~ranking of~~ *LE*

596 values ~~is~~were ranked as follows: OAFlux < MEP < J-OFURO3 < ERA5 < MERRA2, which ~~is~~was consistent

597 with the magnitude of available energy. For sensible heat, MEP-derived H closely ~~resembles~~resembled that

598 of ERA5 and MERRA2, with higher values predominantly occurred in two western boundary current systems,

599 the South Indian Ocean near Australia area, and the Arctic Ocean. The improved MEP method

600 ~~mitigates~~mitigated the issue of overestimating *H* in mid-to-high latitudes compared to its original form

601 (Fig.6l), resulting in a more realistic spatial ~~patterns~~pattern. In high latitudes, J-OFURO3 ~~exhibits~~exhibited

602 higher H values than MEP and other comparable products in the Northern Hemisphere, with negative values

603 observed between 45°S and 55°S. MEP generally ~~estimates~~estimated *H* within an intermediate range

604 compared to other products, displaying a distribution that ~~is~~was more reasonable than that of J-OFURO3

605 product.

606

607

608

609

610 **Table 5.** Global area-averaged multi-annual mean estimates of latent heat flux

LE products	*LE* (W·m^{-2})	Evaporation (mm/yr)	*H* (W·m^{-2})	*G* (W·m^{-2})
MEP (0.24)	92.8	1195.5	12.2	19.7
ERA5	99.2	1277.8	12.0	34.2
MERRA2	100.5	1294.3	13.2	35.5
J-OFURO3	94.9	1222.2	10.1	19.7
OAflux	88.9	1145.1	10.4	/
MEP (ori)	52.7	678.5	25.1	42.2

611 Note: The period spans from 1988 to 2017. The MEP (0.24) denotes the improved MEP model, while MEP
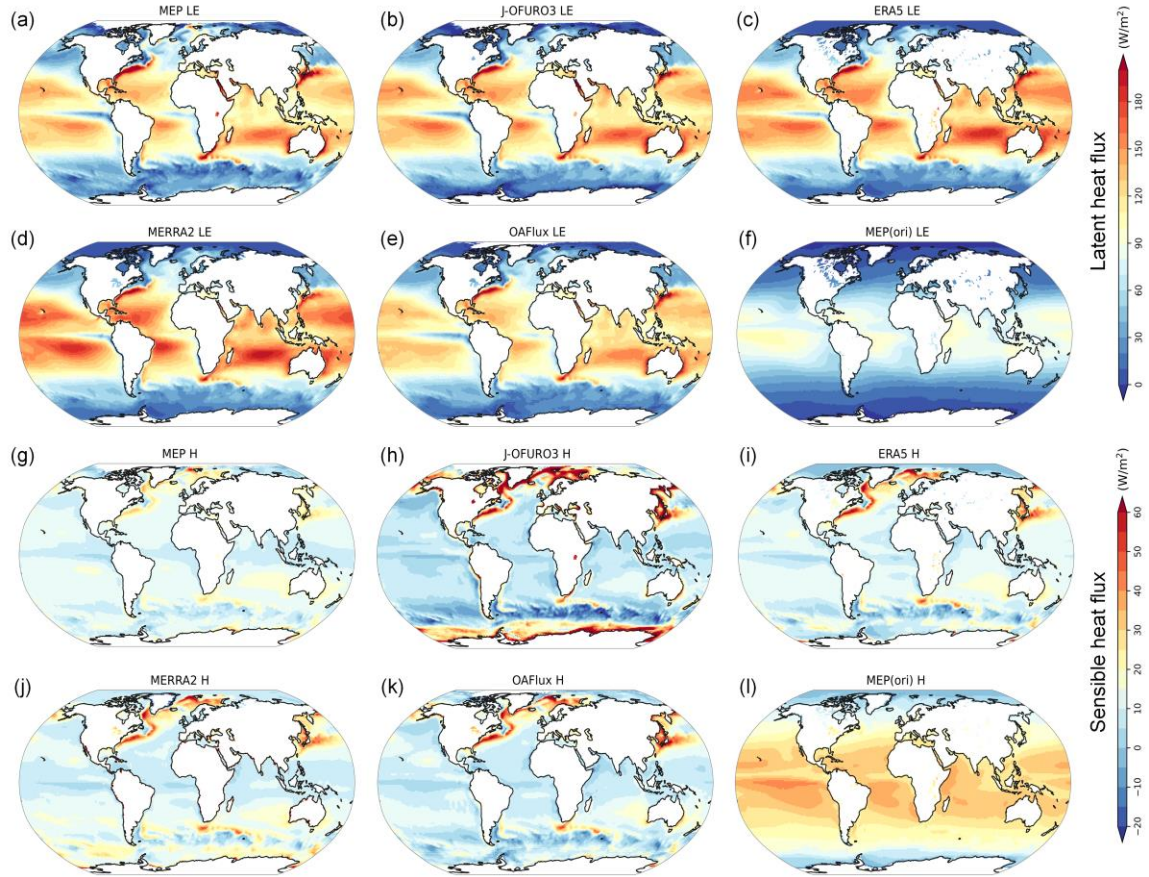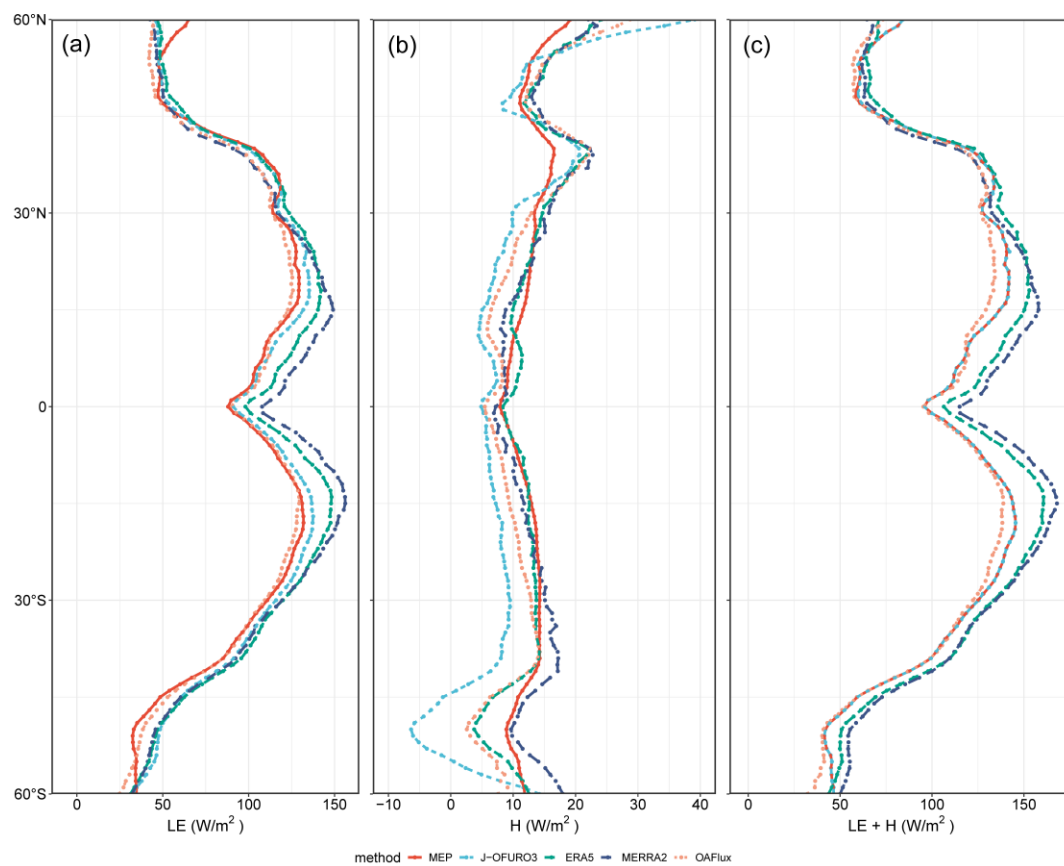612 (ori) represents the original MEP model.
613

Figure 6. Global spatial maps of annual mean latent heat flux (*LE*) and sensible heat flux (*H*) during 1988-2017. Panels (a)-(f) depict latent heat flux derived from the improved MEP method, J-OFURO3, ERA5, MERRA2, OAFlux, and the original MEP method. Panels (g)-(l) show sensible heat flux from the same datasets.
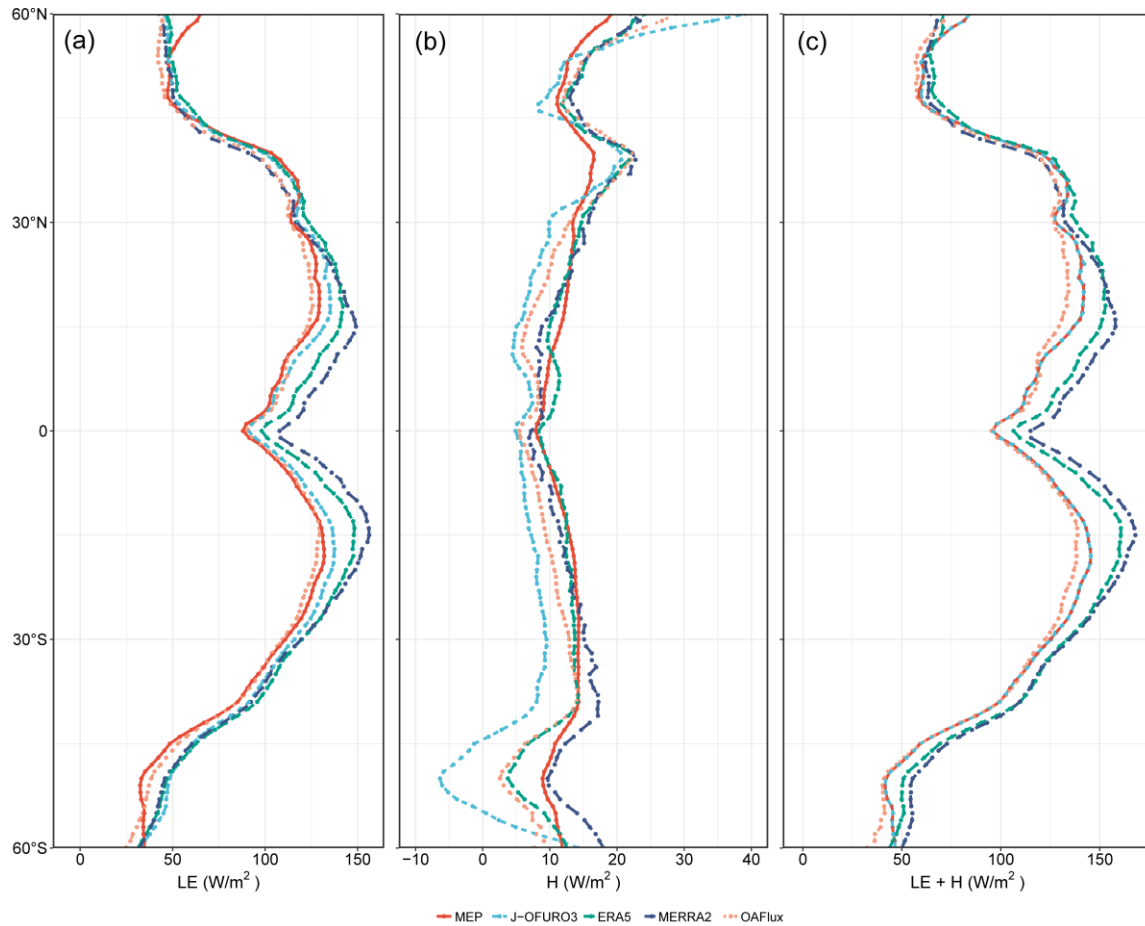
621

Figure 7. Meridional profiles of latent heat (left panel), sensible heat (middle panel) and their sum representing available energy (right panel) for the period 1988-2017~~.~~, produced by MEP, J-OFURO3, ERA5, MERRA2, and OAFlux datasets.

4.4.2 Validation of global latent heat products against the observational sites

To evaluate the ~~disparity~~discrepancies between MEP ~~estimates of~~estimated *LE* and ~~those of~~ other ~~existing~~ ~~products~~datasets, this study validated global-scale *LE* ~~using~~at 129 observational sites (as depicted in Fig.8 & Table 6). MEP-estimated *LE* showed strong consistency with buoy observations, achieving an R^2 of 0.79, a ME of 1.26 $W \cdot m^{-2}$, and RMSE of 16 $W \cdot m^{-2}$, all surpassing those of alternative products, underscoring its superior performance. Moreover, the MEP method exhibited superior performance with a higher NSE value of 0.77 and KGE of 0.89, demonstrating enhanced accuracy, reliability, and robustness. According to the RMSE evaluation criterion, the ranking of best-performed *LE* products ~~is~~was as: MEP, J-OFURO3, OAFlux, ERA5, MERRA2. In a recent comprehensive assessment of 15 global ocean *LE* products (Tang et al., 2023), RMSE values ranged from 17.2 to 45.3 $W \cdot m^{-2}$, in which J-OFURO3 emerged as the best-performing product

637 with the lowest RMSE of 17.2 W·m^{-2}, highest correlation coefficient (R) of 0.89, and ME of 6.5 W·m^{-2}.

638 Studies have also shown minimal bias ~~are~~were given by J-OFURO3 on daily scale (Bentamy et al., 2017).

639 This superior performance of J-OFURO3 dataset can be attributed to the use of continuously updated bulk

640 algorithms (COARE 3.0 version~~) by J-OFURO3,~~), the ongoing optimization of near-surface parameters

641 (Tomita & Kubota, 2018), as well as the improved spatial resolution (0.25°). In this study, the improved MEP

642 ~~estimates~~estimation of *LE* outperformed that of J-OFURO3, demonstrating higher accuracy and lower error

643 (ME=1.26 W·m^{-2}), thereby establishing it as the most accurate global *LE* product currently available.
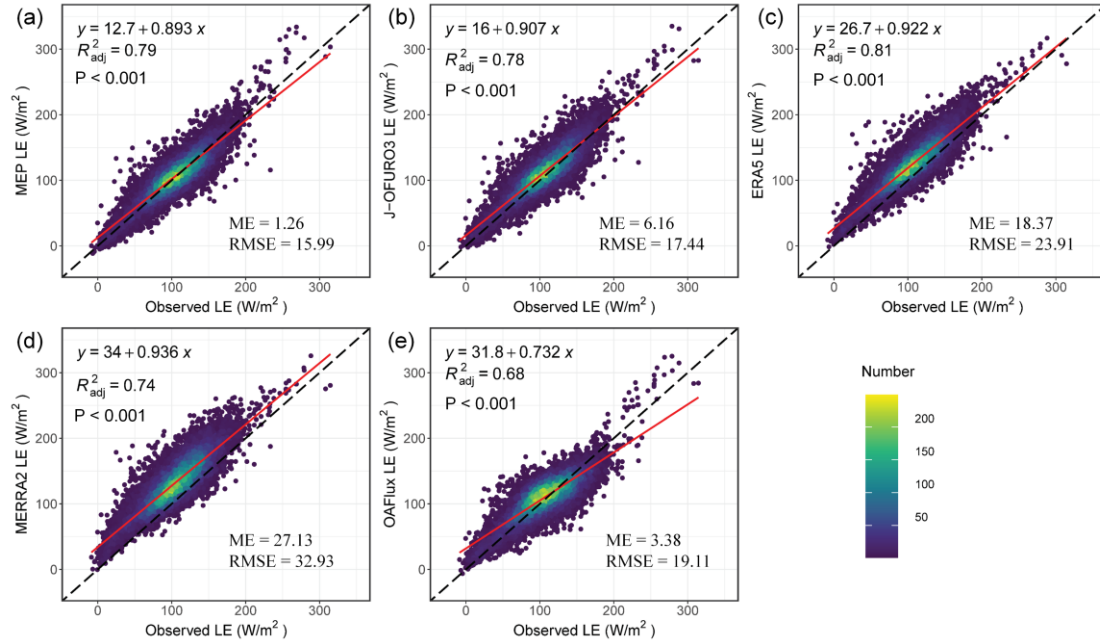

644
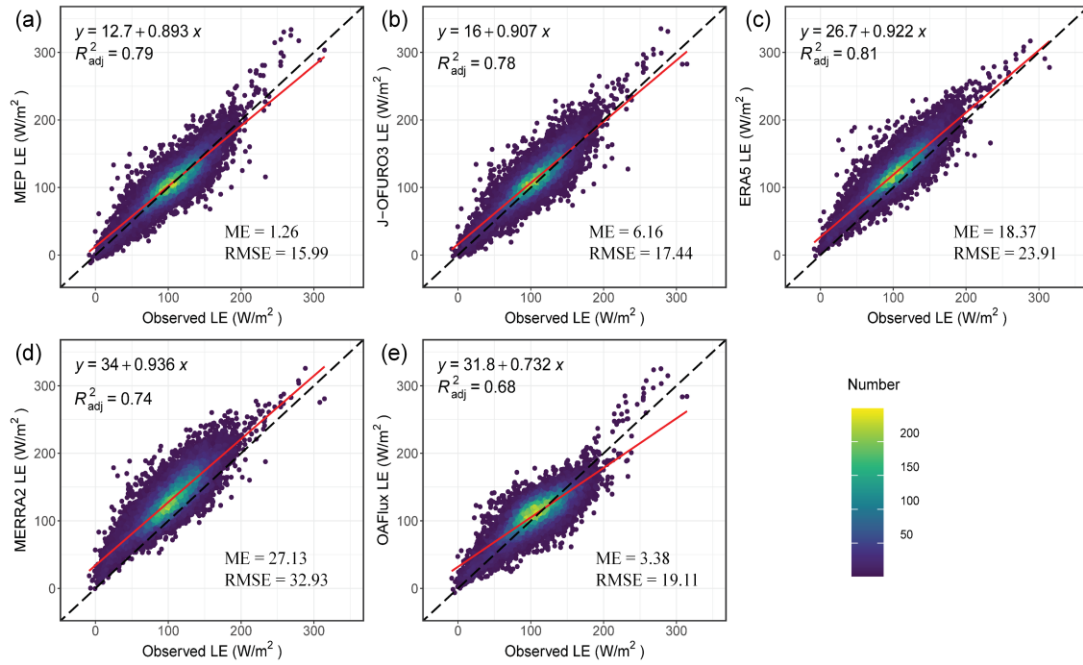
Figure 8. Scatter density plots of latent heat flux ~~derived~~taken from ~~distinct methods~~different products versus observations from 129 buoy stations during the period 1988-2017: (a) Improved MEP ~~method~~model, (b) J-OFURO3, (c) ERA5, (d) MERRA2, and (e) OAFlux. A total of 15444 records of latent heat observations are included.

**Table 6.** Evaluation of latent heat flux from different methods against buoy observations

Products	R^2	ME (W·m^{-2})	MAE (W·m^{-2})	RMSE (W·m^{-2})	PBIAS (%)	NSE	KGE
MEP	0.79	**1.3**	**12.2**	**15.9**	**1.2**	**0.77**	**0.89**
J-OFURO3	0.78	6.3	13.4	17.4	5.8	0.73	0.87
ERA5	**0.81**	18.4	19.9	23.9	17.3	0.48	0.80
MERRA2	0.74	27.1	28.1	32.9	25.5	0.02	0.70
OAFlux	0.68	3.4	14.9	19.1	3.2	0.67	0.79

Note: The evaluation period spans from 1988 to 2017, and the best-performed statistics are indicated in bold type.

4.4.3 Comparisons of Bowen ratios

The improved MEP model ~~achieves~~achieved accurate *LE* ~~estimates~~estimation after refining the process of partitioning the surface energy budget, specifically through revisions to the Bowen ratio. The improved MEP method notably decreased the global-scale Bowen ratio, as illustrated in Fig. 9 and 10. Regarding latitude averages, the Bowen ratio of the original MEP formula ranged from 0.37 to 1.48 (with a median of 0.80), whereas the modified MEP Bowen ratio ranged from 0.09 to 0.35 (median of 0.18). Specifically, in the low-latitude region (10°S-10°N), the Bowen ratio of the modified MEP formula decreased from 0.37 to approximately 0.1, aligning closely with the Bowen ratios obtained from other reanalysis products (MERRA2,

662 ERA5, OAFlux, and J-OFURO3). Globally, the median Bowen ratios of the products ~~are~~were as follows:

663 MERRA2 (0.15), MEP (0.12), ERA5 (0.09), OAFlux (0.08), and J-OFURO3 (0.06). Spatially, the MEP

664 Bowen ratio ~~resembles~~resembled ERA5 in mid to low latitudes but ~~exhibits~~exhibited deviations from other

665 products at high latitudes, where those products ~~show~~showed fluctuating changes in the Bowen ratio (Fig.10).

666 For instance, other products ~~display~~displayed abrupt transitions from negative to positive Bowen ratios in the

667 Arctic and Antarctic regions, whereas MEP-derived values ~~demonstrate~~demonstrated greater stability in

668 variations at higher latitudes. This discrepancy ~~is~~was likely due to the reanalysis products relying on the bulk

669 method, which ~~is~~was sensitive to variations in wind speed and temperature gradients, leading to errors in

670 simulating high wind speeds at the poles and causing fluctuations in latent and sensible heat. In contrast, the

671 MEP model strictly adheres to energy conservation principles and operates independently of wind speed and

672 temperature gradients, resulting in a more accurate estimate of the Bowen ratio. For example (Fig.S9), at the

673 high-latitude PAPA buoy site (144.9°W, 50.1°N), the Bowen ratio estimated by MEP (median 0.24) closely

674 ~~matches~~matched the observed Bowen ratio (median 0.23). In contrast, all the other products underestimated

675 the Bowen ratio, with J-OFURO3 (median -0.09) and OAFlux frequently exhibiting negative values. The

676 Bowen ratio derived from MEP ~~fits~~fit well with a Generalized Additive Model (GAM) (Fig.9). The implicit

677 functional relationship between Bowen ratio and latitude ~~is~~was expressed as ($R^2 = 0.996$, $p < 0.001$): B_{oa} (lat)

678 $= 0.207218 + f(lat) + \varepsilon$, where *f(lat)* represents a smoothing function derived from a smooth curve, and ε

679 denotes the error term. However, the specific functional form of *f(lat)* cannot be explicitly determined.

680 Therefore, a polynomial regression method ~~is~~was employed to explicitly fit B_{oa} and *lat*, resulting in ($R^2 =$

681 0.91, $p < 0.001$): $B_{oa} = 9.97 \times 10^{-2} - 3.45 \times 10^{-4} \times lat + 4.71 \times 10^{-5} \times lat^2 + \varepsilon$ (as in Fig.S10). This equation

682 ~~serves~~can serve as a reference for partitioning surface energy ~~over~~in data-sparse oceanic regions.

684
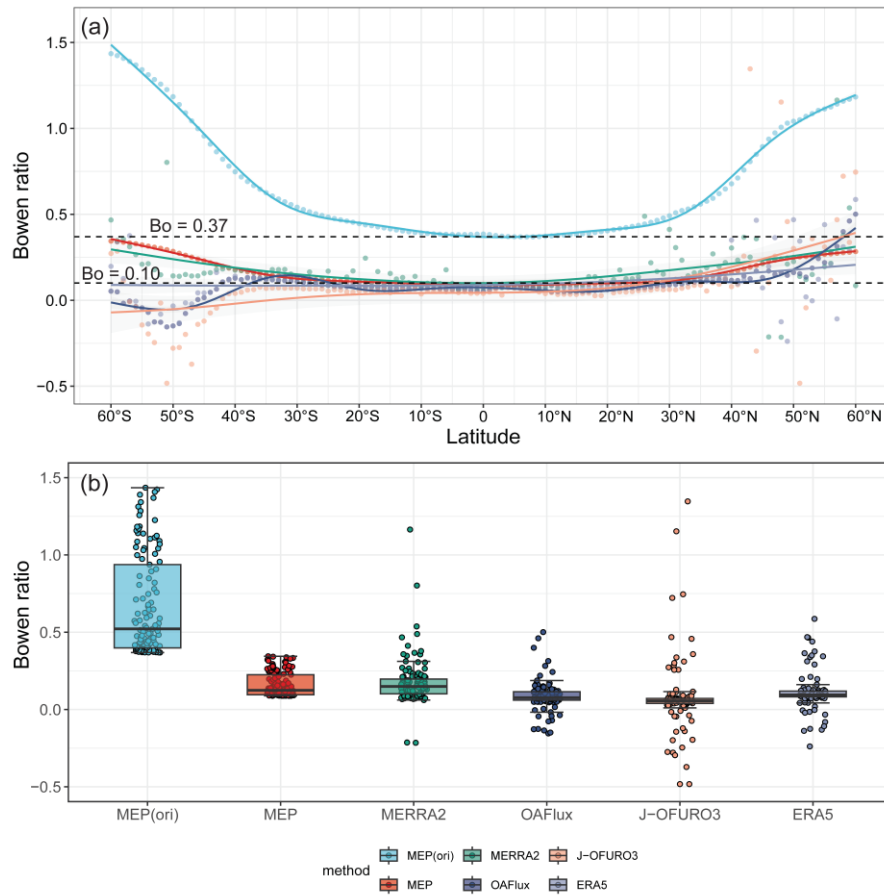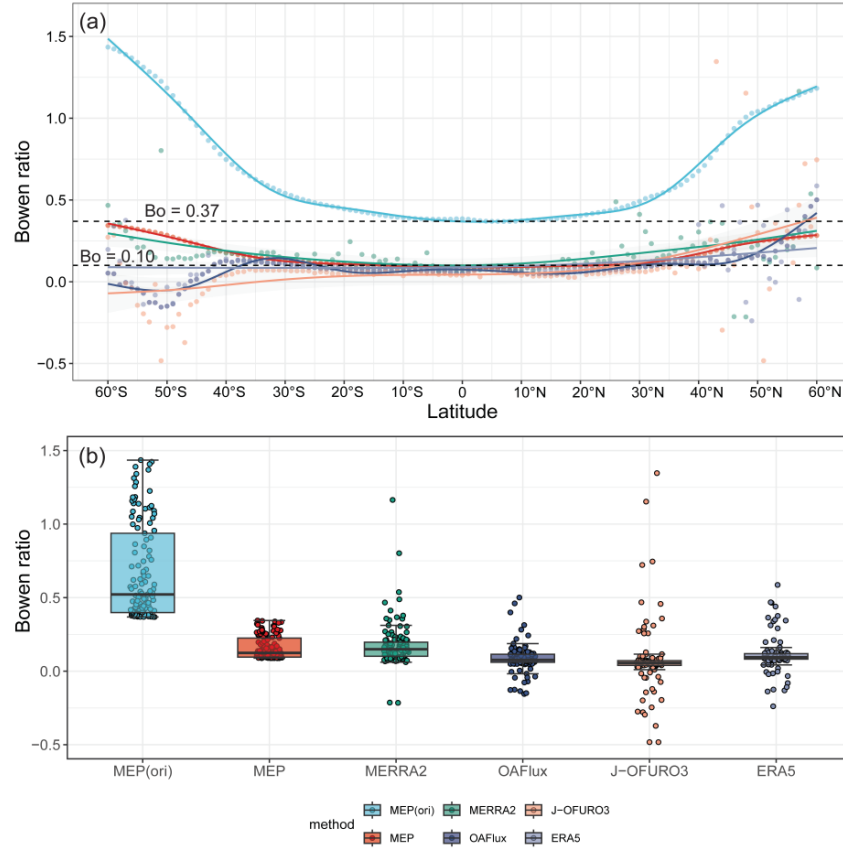
Figure 9. Global ocean latitudinal averaged Bowen ratio derived by the MEP method and four other products from 1988 to 2017. (a) Latitudinal averaged Bowen ratio derived from the MEP model using original and modified Bowen ratio formulas, with points fitted by a generalized additive model (GAM). (b) Statistical distribution of the latitudinal annual mean Bowen ratio.

689

690
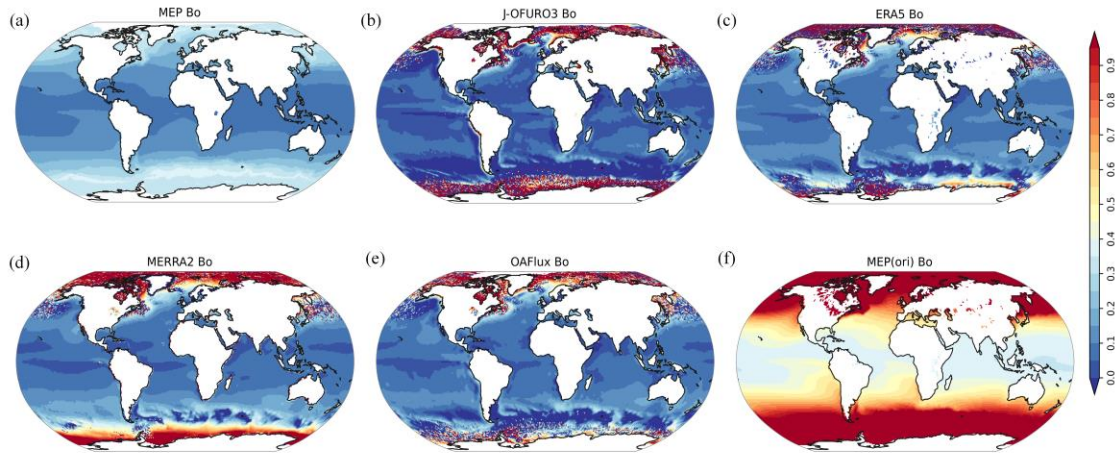
Figure 10. Global distribution of ocean annual mean Bowen ratio during 1988-2017: (a) Improved MEP method, (b) J-OFURO3, (c) ERA5, (d) MERRA2, (e) OAFlux, and (f) MEP original method.

693

4.5 Spatial-temporal variability of ocean evaporation

Heat flux reflects the energy exchange between the ocean and the atmosphere, while evaporation (*ET*) reflects moisture exchange within the water cycle. The spatiotemporal patterns of evaporation were analyzed using the Sen's slope and the Mann-Kendall test methods (Fig. 11). GloballyFor the global ocean, approximately 74% (of the regions showed an increasing trend, with about 27% of the grids exhibiting statistically significant) showed an increasing trend, while increases ($p < 0.05$). In contrast, 26% (displayed a decreasing trend, with 21%only 5% of the grids showing statistically significant) exhibited a decreasing trend. The decrease ($p < 0.05$). For the whole periods, the regions with the highest increasing trends were predominantly observed near western boundary current systems, the convergence zones of the East Australian Current and the South Equatorial Current, and the convergence zones of the Eastern South Equatorial Current and the Brazil Current along South America. Decreasing trends were primarily observed in equatorial regions of the Pacific and Atlantic Oceans, as well as near the Labrador and Kuroshio currents and north of the Antarctic Circle. It iswas indicated that regions with significant increases (decreases) in evaporation generally correspond closely to the distribution of major warm currents (cold currents) spatially. However, global ocean evaporation experienced a notable shift around 2003, as illustrated in Figs.11b and 11c. The downward trend observed from 2003 to 2017 counteracted a significant portion of the growth trend that occurred during the previous 16 years (1988-2003), particularly evident in the mid-latitude regions (15ºS-20ºN). In the middle-to-low latitudes (0º-30ºN), nearly all ocean grids exhibited opposite trends around 2003. Spatially, regions that displayed the largest increasing trends during 1988-2003 transitioned to show the most substantial decreasing trends between 2003 and 2017. This includes regions associated with western boundary current systems, convergence zones of the East Australian Current and the South Equatorial Current, as well as equatorial regions of the Pacific and Atlantic Oceans (Fig. 11c). To further investigate the shift in ocean evaporation after 2003, we analyzed the interannual variability of global annual mean area-weighted evaporation using all available datasets (as shown in Fig.12).

Over the multi-year changesperiod from 1988 and 2017, MEP, J-OFURO3, ERA5, and MERRA2 all exhibited significant increasing trends in *ET*. MEP estimated an evaporation increasedincrease rate of 2.31 mm/year, whereas OAFlux showed a non-significant trend (Fig. 12). This upward trend in ET can largely be attributed to changes in available energy, which increased at a rate of 0.274 W/(m² year). For instance, during

722 ~~peak *ET* years such as 1989, 1992, 2003, and 2008, *R$_n$* was also at its highest; conversely, during years of~~

723 ~~minimum *ET* like 1991 and 1997, *R$_n$* was minimal. This consistency is in line with previous findings (Huang~~

724 ~~et al., 2017), where more than 50% of the uncertainty in MEP-modeled fluxes was attributed to the radiation~~

725 ~~term.~~ While different ~~methods yield~~datasets revealed varying magnitudes of *~~ET~~*evaporation changes, ~~they~~

726 ~~generally exhibit~~most exhibited a ~~transition around 2010~~similar temporal pattern: an increasing trend from

727 1988 to around ~~2010~~2003, followed by a hiatus during 2003-2010, and ultimately a decreasing trend

728 ~~thereafter~~after 2010 (Fig. 12a). ~~For instance~~Specifically, MEP indicated an ~~ET increase~~increasing trend in

729 evaporation of 3.58 mm/year from 1988 to 2010, followed by a decrease ~~at a rate~~of 2.18 mm/year after 2010~~.~~

730 ~~This shift primarily results from a decline in both available energy~~ (Fig. 12a). The slowdown and transition

731 of evaporation during 2003-2010 aligned with the concept of a "global warming hiatus" (Medhaug et al.,

732 2017; Sung et al., 2023), referring to the period when global mean surface air temperatures did not continue

733 to rise between 1988 and 2012. Previous studies have proposed four potential explanations for this global

734 warming hiatus: internal variability, external drivers, the Earth's response to CO_2, and radiative forcing

735 (Medhaug et al., 2017). This study indicates that changes in radiative forcing (Fig. 12b) can significantly

736 affect the interannual variability of evaporation (Fig. 12a) and surface temperature ~~starting around 2010.~~(Fig.

737 12c). This finding is consistent with previous research that attributed more than 50% of the uncertainty in

738 MEP-modeled fluxes to the radiation term (Huang et al., 2017). Although *~~T$_s$~~ ~~increased~~*surface temperature

739 began to increase after 2012, the ~~significant~~decrease in available energy ~~was~~remained the ~~main~~primary driver

740 behind the decline in *~~ET~~*evaporation.

741

ET annual trend

(a) Evaporation trend (1988-2017)

(b) Evaporation trend(1988-2003)
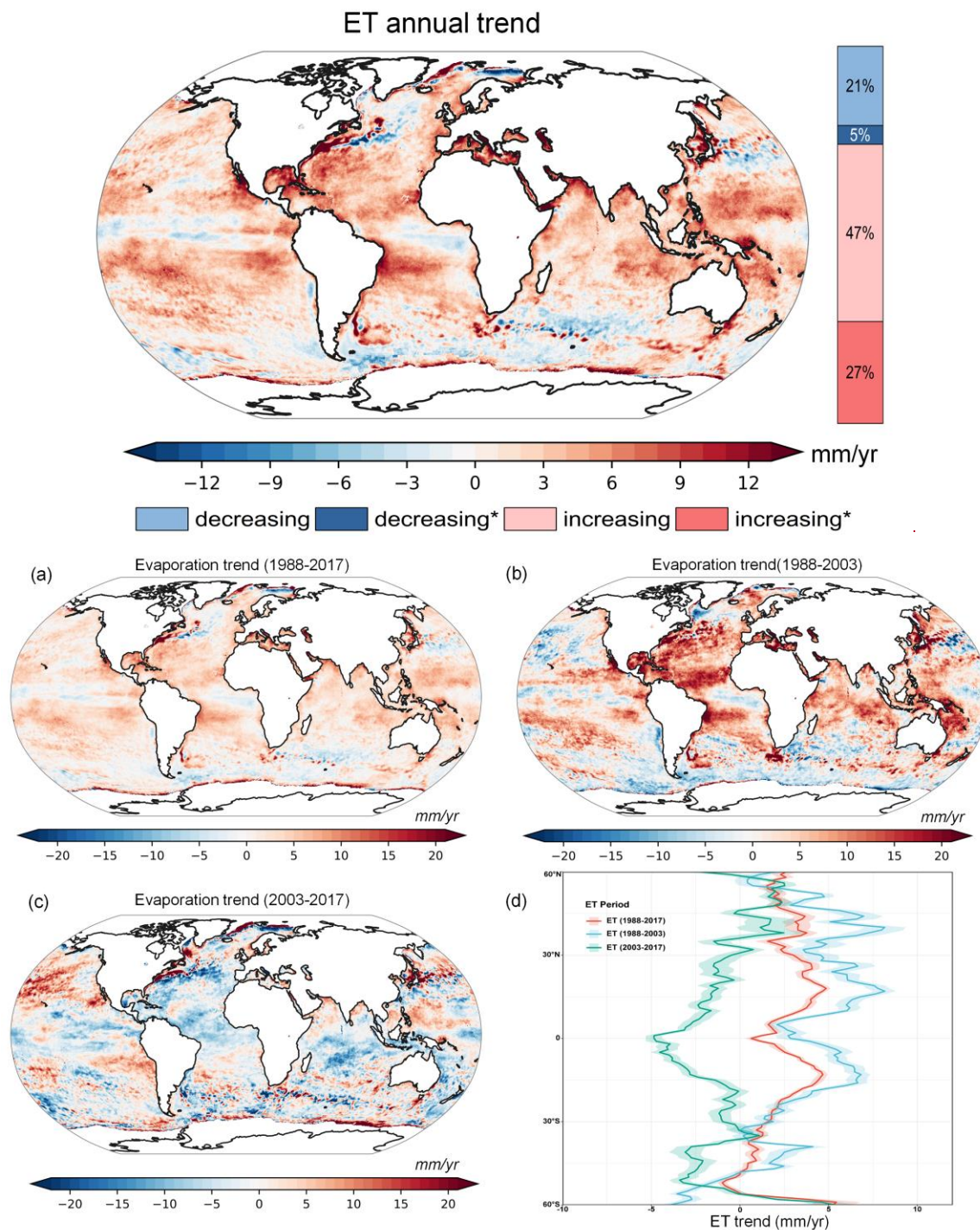
(c) Evaporation trend (2003-2017)

(d)

Figure 11. Spatial distribution of ~~the long term trend in the annual mean~~ multi-year trends in ocean evaporation ~~derived from~~estimated by the improved MEP method during ~~1988-2017~~(a) the period 1988-2017, (b) the period 1988-2003, (c) the period 2003-2017, and (d) the latitudinal average changes across three different periods.
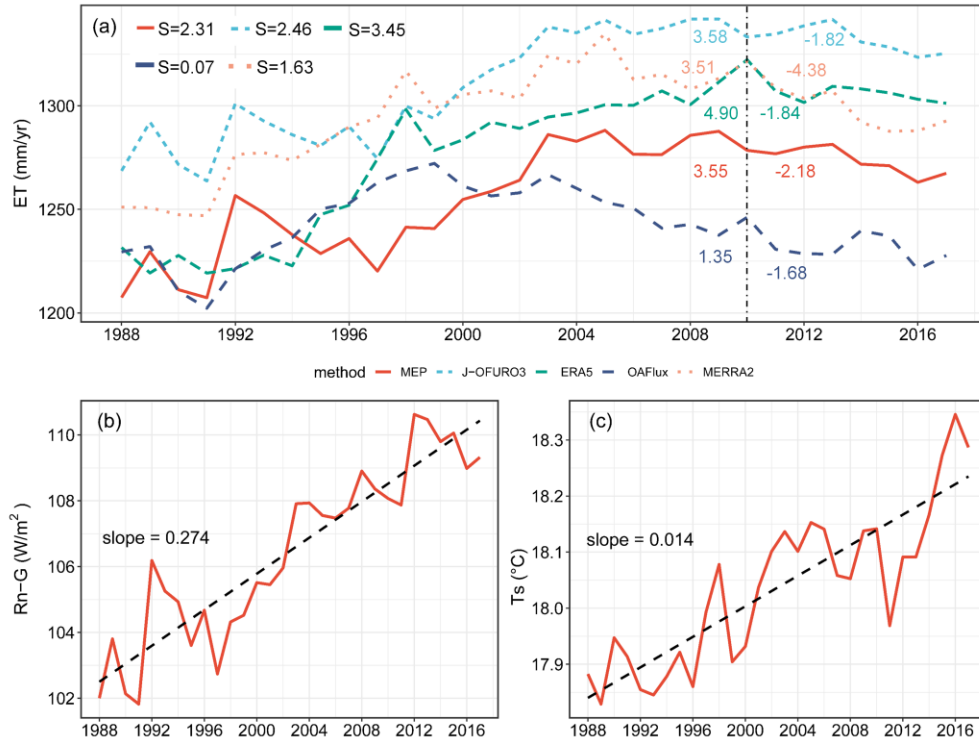
749

Figure 12. Time series of area-averaged multi-annual mean evaporation from the improved MEP method (a), available energy (b), and sea surface temperature (c) over the global oceans during 1988-2017. The black dotted line in panel (a) ~~represents~~marks the year 2010, and the label "S = 2.31" indicates that the MEP-estimated global multi-annual mean evaporation increased at a rate of 2.31 mm/year during 1988-2017, with change rates of different ET datasets represented by various colors. The black dashed lines in panels (b) and (c) ~~represent~~denote the linear regression lines.

5. Discussion

5.1 Quantifying the impact of heat storage and radiation with sensitivity analysis

The sensitivity analysis ~~reveals~~revealed the significant influence of input variables on latent heat flux derived from the MEP model. Notably, the heat storage (G) ~~exhibits~~exhibited seasonal variations with both positive and negative values (Fig. 13). Positive G values ~~coincide~~coincided predominantly with summer in the Northern Hemisphere (winter in the Southern Hemisphere), specifically from June to August (Fig. 4 and Fig. S5). During this season, intensified solar radiation enhances the net energy input (R_n) at the ocean surface, leading to heat absorption and retention. Consequently, the energy available (R_n - G) for evaporation diminishes. The analysis ~~indicates~~indicated that R_n significantly ~~influences~~influenced the energy-driven evaporation process, with a sensitivity coefficient exceeding 1 (median 1.74), highlighting its pivotal role. In contrast, G negatively ~~impacts~~impacted evaporation, as indicated by a sensitivity coefficient of -0.74.

39

767 Specific humidity (median 0.08) and sea surface temperature ~~have~~had relatively minor effects, consistent

768 with previous MEP model findings focused on terrestrial surfaces (Isabelle et al., 2021).

769   Conversely, negative values of heat storage predominate during winter, particularly from December to

770 February in the Northern Hemisphere (June to August in the Southern Hemisphere). Despite reduced solar

771 radiation during this period, residual heat stored from summer gradually releases into the atmosphere,

772 resulting in greater energy output than input. This surplus energy ~~augments~~increases the available energy for

773 evaporation, leading to a positive sensitivity coefficient for G (median 0.29), second only to R_n (median 0.71).

774 Consequently, this process generally reduces sea surface temperature, resulting in a negative sensitivity

775 coefficient for surface temperature. Overall, these findings ~~underscore~~underscored the significant influence

776 of R_n on latent heat flux, with G ranking as the second most influential variable in MEP estimates over ocean

777 surfaces. For instance, a 10% decrease in positive G ~~yields~~yielded a 7.4% increase in evaporation, while a

778 10% increase in negative G ~~results~~resulted in a 2.9% increase in evaporation, assuming other variables remain

779 constant. Thus, R_n and G ~~emerge~~emerged as two primary drivers of oceanic evaporation, with humidity and

780 temperature exerting minimal influence.

781   ~~Furthermore, the pivotal role of available energy in determining *LE* is underscored by its direct~~

782 ~~relationship with energy allocation. Thus, the~~ The accuracy of available energy estimates ~~directly~~

783 ~~influences~~significantly *LE* simulations~~. Despite using~~, as it serves as the direct energy source for partitioning

784 latent and sensible heat fluxes. Although the bulk methods (e.g., COARE 3.0 algorithms) used for estimating

785 heat fluxes are independent of ~~radiation partitioning~~surface energy budget allocation, discrepancies in *LE*

786 ~~simulations~~estimation still correlate ~~with errors~~strongly with validated biases against observations in

787 available energy estimates (see Tables 3 and 4). Notably, the MERRA2 product exhibited higher errors in

788 simulating R_n and G compared to observations, leading to significant biases in *LE* estimation. In contrast, the

789 ERA5 product demonstrated superior performance in simulating R_n and G, thereby achieving higher accuracy

790 in *LE* estimation. Consequently, the energy-balance-based MEP model excels in accurately

791 ~~computing~~estimating surface heat fluxes by directly reflecting energy allocation. Unlike bulk methods, the

792 MEP approach reduces sensitivity to temperature and humidity gradients, thereby minimizing uncertainties

793 in *LE* simulations (Pelletier et al., 2018). This advancement enhances the MEP model's utility in global

794 energy and water cycle research, particularly pertinent for future climate change studies.
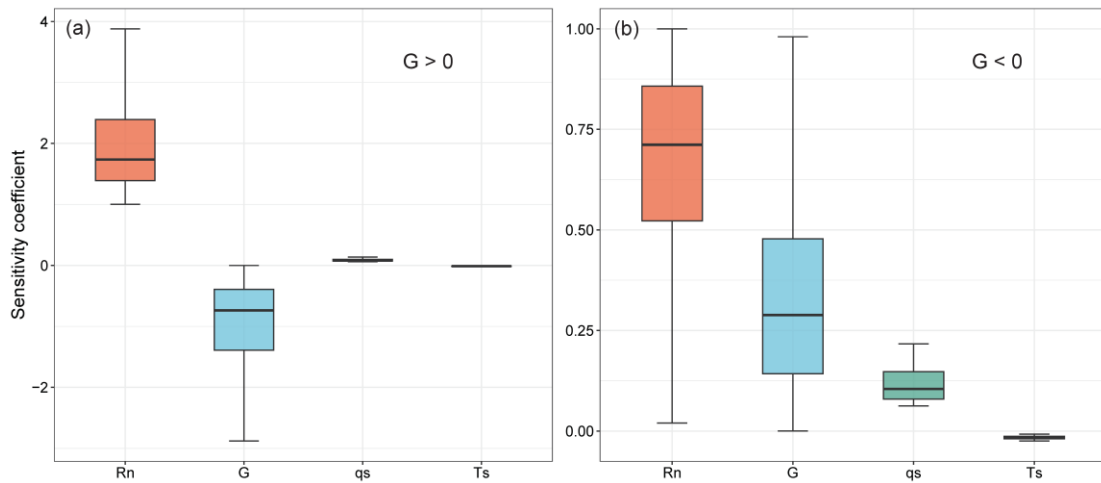
795

Figure 13. Sensitivity coefficient associated with inputs variables for the improved MEP method at all 129 buoy stations: (a) for positive G values, and (b) for negative G values.

5.2 Discrepancy of empirical Bowen ratio formulas

~~Bowen ratio~~B_o plays a crucial role in understanding the surface energy partitioning process. In this study, four empirical formulas were utilized to modify the MEP model and ~~were~~ evaluated against ~~observations of latent heat flux~~the observed LE, each with distinct conditions of applicability and suitability for integration with the MEP model: (1) $B_{oa}=0.63B_o{}^*-0.15$ ~~is~~was derived from direct observational data fitting (Hicks and Hess, 1977). This formula ~~is~~was applicable for surface temperatures above 16°C, particularly within latitudes between 40°N and 40°S, making it more suitable for lower latitude regions~~. Therefore, it is more suitable for lower latitude regions~~; (2) $B_{oa}=0.79B_o{}^*-0.21$ ~~is~~was derived using the Priestley–Taylor model under advection-free conditions (Priestley and Taylor, 1972). The coefficients ~~are~~were determined based on a mean α value of 1.26 ~~(,~~ although this ~~varies~~value can vary in practice~~)~~. ~~However, recent~~. Recent studies have ~~shown~~revealed significant discrepancies due to the neglect of ~~the~~ interaction between ~~R_n and T_s~~variations in R_n and T_s (Yang & Roderick, 2019~~);~~). To address this limitation, the equation (3) $B_{oa}=0.24B_o{}^*$ was developed ~~to address this limitation~~ based on ~~a~~the maximum evaporation theory ~~by~~, considering the feedback ~~mechanism~~mechanisms between R_n and T_s ~~(under the circumstances of~~while assuming that G ~~to be~~is small ~~to~~or negligible~~).~~. The empirical coefficient ~~(~~0.24~~)~~ was determined by fitting ~~Bowen ratio~~B and ~~surface temperature data~~T_s across the global ocean surface (Yang & Roderick, 2019); and (4) $B_{oa}=0.37B_o{}^*-0.05$ was ~~subsequently~~ formulated based on principles derived from atmospheric boundary layer (ABL) theory (Liu &

41

817   Yang, 2021), with coefficients also fitted from relationships between B_{oa} and T_s. It should be noted that the

818   derivations of $B_{oa}=0.24B_o{}^*$ and $B_{oa}=0.37B_o{}^*-0.05$ were based on fitting using ~~latent heat data~~LE from the

819   OAFlux dataset rather than direct buoy observations. ~~Building upon the four empirical relationships between~~

820   ~~B_{oa} and $B_o{}^*$ from previous studies, this study assessed the applicability of these four empirical Bowen ratio~~

821   ~~formulas in estimating latent heat flux. The findings indicate that~~Overall, the MEP model ~~refined~~incorporated

822   with $B_{oa}=0.24B_o{}^*$, ~~exhibits~~exhibited superior accuracy at both localized and global scales, effectively

823   mitigating the underestimation of *LE* in its original ~~formulation. Moreover, the results show that the improved~~

824   ~~MEP model closely aligns with buoy observations and achieves higher accuracy globally compared to~~

825   ~~OAFlux products (as depicted in Fig. 8), surpassing other bulk method-based products as well.~~estimates.

826   ### 5.3 Contributions and implications of this study

827   The main contributions of this study include: (1) The MEP model's energy balance equation over water

828   surfaces was revised to explicitly consider heat storage effect. This correction highlights the importance of

829   heat storage in estimating ~~latent heat flux.~~*LE*. (2) The energy partitioning of the MEP model was revised to

830   incorporate empirical Bowen ratio formulas, significantly improving the heat flux estimations. (3) This study

831   conducted the first thorough global assessment of heat storage using extensive buoy observations and remote

832   sensed data, enabling the MEP model to produce the most accurate global ~~latent heat flux~~*LE* estimates. This

833   study addresses the issue of underestimating ~~latent heat flux~~*LE* by the original MEP model, increasing the

834   global average *LE* from 53 W·m^{-2} to 93 W·m^{-2}, while reducing sensible heat flux from 25 W·m^{-2} to 12 W·m^{-}

835   ^{2}, improving the partitioning of energy budget. The improved MEP model ~~provides~~provided precise *LE*

836   estimates compared to existing datasets like J-OFURO3, ERA5, MERRA2, and OAFlux, enabling it to

837   become a valuable benchmark dataset for global evaporation studies.

838   From a methodological perspective, the improved MEP method ~~presents~~emerged as a ~~new~~novel

839   approach for estimating ~~heat flux~~energy fluxes that diverges from ~~existing~~traditional bulk methods. The

840   conventional bulk method ~~traditionally~~ requires multiple input parameters, including air temperature, specific

841   humidity, wind speed, sea surface temperature, ~~and~~ atmospheric pressure, ~~as well as~~and the observational

842   height of all parameters (~~Fairal~~Fairall et al., 2003; Tomita et al., 2021). ~~In contrast to the bulk~~This method,

843   ~~which requires a high demand for driving~~ demands numerous input variables, ~~and shows lower sensitivity~~

844   ~~to~~the estimated fluxes are highly sensitive to changes in temperature ~~variations. It~~and humidity gradients. In

845 contrast, the improved MEP model requires only net radiation, heat storage, and surface temperature, and

846 atmospheric pressure to simultaneously estimateobtain latent heat and sensible heat fluxes, making it more

847 flexible to operate and robust against variations in input variables. Furthermore, the improved MEP model is

848 not constrained by the magnitude of heat storage and theoretically can be applied across various temporal

849 scales (including sub-daily and daily), beyond the monthly scale used in this study. This underscores the

850 applicability of the MEP method in addressing the constraints of traditional bulk methods, providing another

851 independent approach to estimating heat fluxes across diverse environmental conditions.

852   This study appliesapplied the improved MEP model to ocean surface, with potential for future extension

853 to lake and reservoir surfaces. Compared to the Penman model for water body evaporation (Tian et al., 2022;

854 Zhao et al., 2022; Bai et al., 2023), the major advantage of MEP method lies in its independence from wind

855 speed, as long as theprovided that heat storage can be determined using an equilibrium temperature-based

856 approach (McMahon et al., 2013; Zhao & Gao, 2019). The global *LE* dataset generated in this study, givendue

857 to MEP's insensitivity to variations in air temperature and humidity, can be applied in studiesresearch related

858 to ocean salinity (Liu et al., 2019), ocean warming (Cheng et al., 2022), and global climate change and water

859 cycle researchstudies (Konapala et al., 2020).

5.4 Limitations

861 The improved MEP method proposed in this study offers a novel approach for estimating ocean heat fluxes,

862 producing a validated long-term global dataset with high accuracy and spatiotemporal continuity. Despite its

863 advancements, the proposed MEP method has several limitations that require further refinement: (1)

864 Uncertainty of Driving data: The input variables of net radiation, heat storage, and sea surface temperature

865 for the MEP model were sourced from the state-of-the-art satellite-based J-OFURO3 dataset. This dataset

866 was constructed using observations from multiple satellite sensors. The net radiation in J-OFURO3 was

867 derived by combining data from the CERES and the International Satellite Cloud Climatology Project

868 (ISCCP) via the creeping sea fill method, along with twelve global sea surface temperature products (Tomitta,

869 2019). Consequently, the uncertainty of the MEP-estimated fluxes may arise from biases in input data derived

870 from various satellite sensors and their associated analysis methods. Therefore, it is essential to integrate

871 multiple approaches to assess the uncertainty associated with the input datasets. Moreover, due to the limited

872 temporal duration of the J-OFURO3 dataset, future work should utilize input datasets with longer time series,

873   finer spatio-temporal resolution (Liang et al., 2022), and higher accuracy to advance ocean heat flux

874   estimations using the MEP method. (2) Heat Storage Determination: This study did not employ a direct

875   calculation method to obtain heat storage. Given the unclear relationship between heat storage and changes

876   in ocean heat content at varying depths (as shown in Table 4), we utilized an energy balance residual-based

877   approach to indirectly estimate heat storage. Consequently, this may render the MEP method susceptible to

878   uncertainties in heat storage data derived from auxiliary flux datasets. Future research should focus on

879   understanding the relationship between ocean heat content changes in the upper 100m and heat storage, with

880   the goal of establishing a functional relationship between water column temperature at different depths and

881   heat storage. (3) Bowen Ratio Improvement: Accurate determination of the Bowen ratio in high-latitude

882   regions remains challenging. The Bowen ratio derived from the MEP method showed significant

883   discrepancies with other datasets in these areas (Fig. 10), particularly in sea-ice-covered Arctic regions, where

884   other datasets exhibited notable overestimations and irregular fluctuations. Therefore, incorporating more

885   observational data from high-latitude regions is essential for a better understanding of energy partitioning

886   patterns.

6. Data availability

888   The GOHF-MEP dataset produced ~~using~~by the MEP method, which includes global latent heat flux and

889   sensible heat flux at a monthly scale from 1988 to 2017, can be freely downloaded from the Figshare platform

890   (https://doi.org/10.6084/m9.figshare.26861767.v2, Yang et al., 2024). All the datasets used in this study are

891   publicly available online and are described in the "Data Materials" section.

7. Conclusions

893   In this study, we developed a new global ~~monthly latent~~ ocean heat flux product ~~for the ocean~~ (GOHF-MEP)

894   covering the period from 1988 to 2017. This product is ~~based on~~grounded in a maximum entropy production

895   theory framework, incorporating heat storage impacts and Bowen ratio ~~optimizations. It~~adjustments. GOHF-

896   MEP represents the first energy-balance-based dataset that ~~differs~~diverges from existing global ocean heat

897   flux datasets derived from bulk methods. To assess the accuracy of the input variables for the maximum

898   entropy production framework, we utilized five global datasets, including two remote sensing-based and

44

899 three from reanalysis-based, ~~alongside~~along with four global datasets of heat storage derived from the energy

900 balance equation and ocean heat content changes. We employed data fusion methods, including arithmetic

901 averaging and the Bayesian three-cornered hat method, to identify optimal input datasets through validation

902 against observations. The performance of the newly produced GOHF-MEP dataset was evaluated against

903 extensive observations from 129 globally distributed buoy stations using multiple statistical metrics~~, and it~~.

904 It was also compared with four auxiliary products: J-OFURO3, ERA5, MERRA2, and OAFlux.

905 ~~Additionally~~Moreover, we analyzed the long-term spatial-temporal variability of ocean latent heat flux.

906 Ultimately, we investigated the impacts of ocean heat storage, net radiation, and Bowen ratio changes on heat

907 flux estimations and surface energy partitioning.

908   The MEP framework provides new estimates of global heat fluxes. The MEP-estimated long-term

909 annual mean latent heat flux is 93 $W \cdot m^{-2}$ (equivalent to 1196 mm/year of evaporation) during the period from

910 1988 to 2017. This estimate is ~~at an~~ intermediate ~~level~~ compared to other global flux products, which range

911 from 90 $W \cdot m^{-2}$ (OAFlux) to 101 $W \cdot m^{-2}$ (MERRA2). The MEP-estimated sensible heat flux is 12 $W \cdot m^{-2}$,

912 falling within the range of 10.17 $W \cdot m^2$ (J-OFURO3) to 13 $W \cdot m^2$ (MERRA2) reported by other current

913 products. Compared with previous heat flux products, the MEP-estimated latent heat demonstrated higher

914 accuracy when validated against observations, with a ME of 1.26 $W \cdot m^{-2}$, a RMSE of 16 $W \cdot m^{-2}$, and a KGE

915 value of 0.89, outperforming all other contemporary global products. Approximately 74% of oceanic regions

916 experienced an increasing trend in evaporation from 1988 to 2017. ~~Regarding~~In terms of long-term temporal

917 variability, the global annual mean evaporation exhibited an increase rate of 3.58 mm/~~yr~~year from 1988 to

918 2010 but subsequently ~~decreased~~declined at a rate of 2.18 mm/~~yr~~year from 2010 to 2017, which was

919 consistent with changes in surface available energy.

920   This study demonstrates that the improved MEP framework has significantly improved the accuracy of

921 the original MEP theory, addressing both the underestimation of latent heat and the overestimation of sensible

922 heat flux. This improvement was achieved by incorporating the impact of heat storage and modifying the

923 Bowen ratio formula within the MEP theory. The consideration of heat storage resolved the issue of seasonal

924 phase mismatches (approximately 6-month lags) between MEP estimates and buoy observations. Building

925 upon this improvement, this study further optimized the energy partitioning process by correcting the Bowen

926 ratio, linearly adjusting the equilibrium Bowen ratio to align with actual conditions. Four empirical Bowen

927 ratio formulas for modifying the MEP method were assessed globally, identifying $B_{oa}=0.24B_o^*$ as the most

928 accurate formula for estimating latent heat flux within MEP method. The impact of heat storage on estimating

929 heat fluxes was quantified through ~~the~~ sensitivity analysis. Net radiation and heat storage were identified as

930 the primary drivers of evaporation estimates. A 10% decrease in positive heat storage led to a 7.4% increase

931 in evaporation, whereas a 10% increase in negative heat storage resulted in a 2.9% increase.

932   Compared to existing bulk methods, the MEP model offers several advantages, including the

933 ~~need~~requirement for fewer input variables, independence from wind speed, and insensitivity to variations in

934 temperature and humidity. The MEP--derived ocean heat flux dataset has been validated and provides

935 accurate estimates of latent heat flux. Additionally, this MEP method can be applied to estimate evaporation

936 from other deep-water surfaces, such as lakes and reservoirs where heat storage is significant. Overall, the

937 MEP-derived ocean heat flux dataset provides high global accuracy, fine spatial resolution (0.25°), and

938 extensive long-term temporal records. This dataset is expected to be valuable for applications related to global

939 ocean warming, hydrological cycles, and their interactions with other Earth system components in the context

940 of climate change.

941

942

943 **Supplement.** The Supplementary material related to this article is submitted during submission.

944

945 **Author contributions.** YY and HS developed the methodology and designed the experiments, WZ

946 contributed the conceptual design, YY and WZ collected and processed the data, YY wrote the first draft of

947 the paper under the supervision of other authors. All authors participated in the ~~revies~~revising and editing of

948 the ~~paper~~manuscript.

949

950 **Competing interests.** The contact author has declared that none of the authors has any competing interests.

951

References

958

959 Andreas, E. L., & Cash, B. A.: A new formulation for the Bowen ratio over saturated surfaces. Journal of
960 Applied Meteorology and Climatology, 35(8), 1279-1289, https://doi.org/10.1175/1520-
961 0450(1996)035%3C1279:ANFFTB%3E2.0.CO;2, 1996.

962 Andreas, E. L., Jordan, R. E., Mahrt, L., & Vickers, D.: Estimating the Bowen ratio over the open and ice-
963 covered ocean. Journal of Geophysical Research: Oceans, 118(9), 4334-4345,
964 https://doi.org/10.1002/jgrc.20295, 2013.

965 Andreas, E. L., Persson, P. O. G., & Hare, J. E.: A bulk turbulent air–sea flux algorithm for high-wind, spray
966 conditions. Journal of Physical Oceanography, 38(7), 1581-1596,
967 https://doi.org/10.1175/2007JPO3813.1, 2008.

968 Bai, P., & Guo, X.: Development of a 60-year high-resolution water body evaporation dataset in China.
969 Agricultural and Forest Meteorology, 334, 109428, https://doi.org/10.1016/j.agrformet.2023.109428,
970 2023.

971 Bai, P., & Wang, Y.: The importance of heat storage for estimating lake evaporation on different time scales:
972 Insights from a large shallow subtropical lake. Water Resources Research, 59, e2023WR035123.
973 https://doi.org/10.1029/2023WR035123, 2023.

974 Bentamy, A., Piolle, J. F., Grouazel, A., Danielson, R., Gulev, S., Paul, F., ... & Josey, S. A.: Review and
975 assessment of latent and sensible heat flux accuracy over the global oceans. Remote Sensing of
976 Environment, 201, 196-218, https://doi.org/10.1016/j.rse.2017.08.016, 2017.

977 Beven, K.: A sensitivity analysis of the Penman-Monteith actual evapotranspiration estimates. Journal of
978 Hydrology, 44(3–4), 169-190, https://doi.org/10.1016/0022-1694(79)90130-6, 1979.

979 Bosilovich, M. G., Robertson, F. R., & Chen, J.: Global energy and water budgets in MERRA. Journal of
980 Climate, 24(22), 5721-5739, https://doi.org/10.1175/2011JCLI4175.1, 2011.

981 Bourras, D.: Comparison of five satellite-derived latent heat flux products to moored buoy data. Journal of
982 Climate, 19(24), 6291-6313, https://doi.org/10.1175/JCLI3977.1, 2006.

983 Chen, X., Yao, Y., Li, Y., Zhang, Y., Jia, K., Zhang, X., ... & Guo, X.: ANN-based estimation of low-latitude
984 monthly ocean latent heat flux by ensemble satellite and reanalysis products. Sensors, 20(17), 4773,
985 https://doi.org/10.3390/s20174773, 2020.

986 Cheng, L., Pan, Y., Tan, Z., Zheng, H., Zhu, Y., Wei, W., ... & Zhu, J.: IAPv4 ocean temperature and ocean
987 heat content gridded dataset. Earth System Science Data Discussions, 1-56,
988 https://doi.org/10.5194/essd-16-3517-2024, 2024.

989 Cheng, L., Trenberth, K. E., Fasullo, J., Boyer, T., Abraham, J., & Zhu, J.: Improved estimates of ocean heat
990 content from 1960 to 2015. Science Advances, 3(3), e1601545, https://doi.org/10.1126/sciadv.1601545,
991 2017.

992 Cheng, L., von Schuckmann, K., Abraham, J. P., Trenberth, K. E., Mann, M. E., Zanna, L., ... & Lin, X.: Past
993 and future ocean warming. Nature Reviews Earth & Environment, 3(11), 776-794,
994 https://doi.org/10.1038/s43017-022-00345-1, 2022.

995 Duan, S. B., Zhou, S., Li, Z. L., Liu, X., Chang, S., Liu, M., ... & Shang, G.: Improving monthly mean land
996   surface temperature estimation by merging four products using the generalized three-cornered hat
997   method and maximum likelihood estimation. Remote Sensing of Environment, 302, 113989,
998   https://doi.org/10.1016/j.rse.2023.113989, 2024.

999 Fairall, C. W., Bradley, E. F., Hare, J. E., Grachev, A. A., & Edson, J. B.: Bulk parameterization of air–sea
1000   fluxes: Updates and verification for the COARE algorithm. Journal of climate, 16(4), 571-591,
1001   https://doi.org/10.1175/1520-0442(2003)016%3C0571:BPOASF%3E2.0.CO;2, 2003.

1002 Fairall, C. W., Bradley, E. F., Rogers, D. P., Edson, J. B., & Young, G. S.: Bulk parameterization of air-sea
1003   fluxes for tropical ocean-global atmosphere coupled-ocean atmosphere response experiment. Journal of
1004   Geophysical Research: Oceans, 101(C2), 3747-3764, https://doi.org/10.1029/95JC03205, 1996.

1005 Gelaro, R., McCarty, W., Suárez, M. J., Todling, R., Molod, A., Takacs, L., ... & Zhao, B.: The modern-era
1006   retrospective analysis for research and applications, version 2 (MERRA-2). Journal of climate, 30(14),
1007   5419-5454, https://doi.org/10.1175/JCLI-D-16-0758.1, 2017.

1008 Guo, J., Li, W., Chang, X., Zhu, G., Liu, X., & Guo, B.: Terrestrial water storage changes over Xinjiang
1009   extracted by combining Gaussian filter and multichannel singular spectrum analysis from GRACE.
1010   Geophysical Journal International, 213(1), 397-407, https://doi.org/10.1093/gji/ggy006, 2018.

1011 He, X., Xu, T., Xia, Y., Bateni, S. M., Guo, Z., Liu, S., ... & Zhao, J.: A Bayesian three-cornered hat (BTCH)
1012   method: improving the terrestrial evapotranspiration estimation. Remote Sensing, 12(5), 878,
1013   https://doi.org/10.3390/rs12050878, 2020.

1014 Hersbach, H., Bell, B., Berrisford, P., Hirahara, S., Horányi, A., Muñoz-Sabater, J., ... & Thépaut, J. N.: The
1015   ERA5 global reanalysis. Quarterly Journal of the Royal Meteorological Society, 146(730), 1999-2049,
1016   https://doi.org/10.1002/qj.3803, 2020.

1017 Hicks, B. B., & Hess, G. D.: On the Bowen ratio and surface temperature at sea. Journal of physical
1018   oceanography, 7(1), 141-145, https://doi.org/10.1175/1520-
1019   0485(1977)007%3C0141:OTBRAS%3E2.0.CO;2, 1977.

1020 Huang, S. Y., Deng, Y., & Wang, J.: Revisiting the global surface energy budgets with maximum-entropy-
1021   production model of surface heat fluxes. Climate Dynamics, 49, 1531-1545,
1022   https://link.springer.com/article/10.1007/s00382-016-3395-x, 2017.

1023 Isabelle, P. E., Viens, L., Nadeau, D. F., Anctil, F., Wang, J., & Maheu, A.: Sensitivity analysis of the
1024   maximum entropy production method to model evaporation in boreal and temperate forests.
1025   Geophysical Research Letters, 48(13), e2020GL091919, https://doi.org/10.1029/2020GL091919, 2021.

1026 Iwasaki, S., Kubota, M., & Watabe, T.: Assessment of various global freshwater flux products for the global
1027   ice-free oceans. Remote sensing of environment, 140, 549-561,
1028   https://doi.org/10.1016/j.rse.2013.09.026, 2014.

1029 Jo, Y. H., Yan, X. H., Pan, J., He, M. X., & Liu, W. T.: Calculation of the Bowen ratio in the tropical Pacific
1030   using sea surface temperature data. Journal of Geophysical Research: Oceans, 107(C9), 17-1,
1031   https://doi.org/10.1029/2001JC001150, 2002.

Johnson, G. C., & Lyman, J. M.: Warming trends increasingly dominate global ocean. Nature Climate Change, 10(8), 757-761, https://doi.org/10.1038/s41558-020-0822-0, 2020.

Konapala, G., Mishra, A. K., Wada, Y., & Mann, M. E.: Climate change will affect global water availability through compounding changes in seasonal precipitation and evaporation. Nature communications, 11(1), 3044, https://doi.org/10.1038/s41467-020-16757-w, 2020.

Lenhart, T., Eckhardt, K., Fohrer, N., & Frede, H. G.: Comparison of two different approaches of sensitivity analysis. Physics and Chemistry of the Earth, Parts A/B/C, 27(9-10), 645-654, https://doi.org/10.1016/S1474-7065(02)00049-9, 2002.

Li, Z., England, M. H., & Groeskamp, S.: Recent acceleration in global ocean heat accumulation by mode and intermediate waters. Nature Communications, 14(1), 6888, https://doi.org/10.1038/s41467-023-42468-z, 2023.

Liang, H., Jiang, B., Liang, S., Peng, J., Li, S., Han, J., ... & Zhang, X.: a global long-term ocean surface daily/0.05 net radiation product from 1983–2020. Scientific Data, 9(1), 337, https://doi.org/10.1038/s41597-022-01419-x, 2022.

Liu, C., Liang, X., Ponte, R. M., Vinogradova, N., & Wang, O.: Vertical redistribution of salt and layered changes in global ocean salinity. Nature communications, 10(1), 3445, https://doi.org/10.1038/s41467-019-11436-x, 2019.

Liu, J., Chai, L., Dong, J., Zheng, D., Wigneron, J. P., Liu, S., ... & Lu, Z.: Uncertainty analysis of eleven multisource soil moisture products in the third pole environment based on the three-corned hat method. Remote sensing of environment, 255, 112225, https://doi.org/10.1016/j.rse.2020.112225, 2021.

Liu, Z., & Yang, H.: Estimation of water surface energy partitioning with a conceptual atmospheric boundary layer model. Geophysical Research Letters, 48(9), e2021GL092643, https://doi.org/10.1029/2021GL092643, 2021.

Long, D., Pan, Y., Zhou, J., Chen, Y., Hou, X., Hong, Y., ... & Longuevergne, L.: Global analysis of spatiotemporal variability in merged total water storage changes using multiple GRACE products and global hydrological models. Remote sensing of environment, 192, 198-216, https://doi.org/10.1016/j.rse.2017.02.011, 2017.

Marti, F., Blazquez, A., Meyssignac, B., Ablain, M., Barnoud, A., Fraudeau, R., ... & Benveniste, J.: Monitoring the ocean heat content change and the Earth energy imbalance from space altimetry and space gravimetry. Earth System Science Data, 14(1), 229-249, https://doi.org/10.5194/essd-14-229-2022, 2022.

Masson-Delmotte V, Zhai P, Pirani S, Connors C, Péan S, Berger N, et al.: IPCC, 2021: Summary for policymakers. in: Climate change 2021: The physical science basis. contribution of working group I to the sixth assessment report of the intergovernmental panel on climate change, pp.3−32, doi:10.1017/9781009157896.001, 2021.

McMahon, T. A., Peel, M. C., Lowe, L., Srikanthan, R., & McVicar, T. R.: Estimating actual, potential, reference crop and pan evaporation using standard meteorological data: a pragmatic synthesis.

Hydrology and Earth System Sciences, 17(4), 1331-1363, https://doi.org/10.5194/hess-17-1331-2013, 2013.

Medhaug, I., Stolpe, M. B., Fischer, E. M., & Knutti, R.: Reconciling controversies about the 'global warming hiatus'. Nature, 545 (7652), 41-47, https://doi.org/10.1038/nature22315, 2017.

Meehl, G. A.: A calculation of ocean heat storage and effective ocean surface layer depths for the Northern Hemisphere. Journal of physical oceanography, 14(11), 1747-1761, ~~https://doi.org/10.1175/1520-0485(1984)014%3C1747:ACOOHS%3E2.0.CO;2, 1984.~~

~~Pelletier, C.,~~https://doi.org/10.1175/1520-0485(1984)014<1747:ACOOHS>2.0.CO;2, 1984.

Morton, F. I.: Evaporation research—a critical review and its lessons for the environmental sciences. Critical Reviews in Environmental Science and Technology, 24(3), 237–280. https://doi.org/10.1080/10643389409388467, 1994.

Pelletier, C., Lemarié, F., & Blayo, E.: Sensitivity analysis and metamodels for the bulk parametrization of turbulent air–sea fluxes. Quarterly Journal of the Royal Meteorological Society, 144(712), 658-669, https://doi.org/10.1002/qj.3233, 2018.

Philip, J.R.: A physical bound on the Bowen ratio. Journal of Climate and Applied Meteorology, 26, 1043–1045, https://doi.org/10.1175/1520-0450(1987)026%3C1043:APBOTB%3E2.0.CO;2, 1987.

Pinker, R. T., & Laszlo, I.: Modeling surface solar irradiance for satellite applications on a global scale. Journal of Applied Meteorology and Climatology, 31(2), 194-211, https://doi.org/10.1175/1520-0450(1992)031%3C0194:MSSIFS%3E2.0.CO;2, 1992.

Pokhrel, S., Dutta, U., Rahaman, H., Chaudhari, H., Hazra, A., Saha, S. K., & Veeranjaneyulu, C.: Evaluation of different heat flux products over the tropical Indian Ocean. Earth and Space Science, 7(6), e2019EA000988, https://doi.org/10.1029/2019EA000988, 2020.

Priestley, C. H. B., & Taylor, R. J.: On the assessment of surface heat flux and evaporation using large-scale parameters. Monthly weather review, 100(2), 81-92, https://doi.org/10.1175/1520-0493(1972)100%3C0081:OTAOSH%3E2.3.CO;2, 1972.

Robertson, F. R., Roberts, J. B., Bosilovich, M. G., Bentamy, A., Clayson, C. A., Fennig, K., ... & Slivinski, L. C.: Uncertainties in ocean latent heat flux variations over recent decades in satellite-based estimates and reduced observation reanalyses. Journal of Climate, 33(19), 8415-8437, https://doi.org/10.1175/JCLI-D-19-0954.1, 2020.

Roderick, M. L., Sun, F., Lim, W. H., & Farquhar, G. D.: A general framework for understanding the response of the water cycle to global warming over land and ocean. Hydrology and Earth System Sciences, 18(5), 1575-1589, https://doi.org/10.5194/hess-18-1575-2014, 2014.

Rutan, D. A., Kato, S., Doelling, D. R., Rose, F. G., Nguyen, L. T., Caldwell, T. E., & Loeb, N. G.: CERES synoptic product: Methodology and validation of surface radiant flux. Journal of Atmospheric and Oceanic Technology, 32(6), 1121-1143, https://doi.org/10.1175/JTECH-D-14-00165.1, 2015.

Shaman, J., & Kohn, M.: Absolute humidity modulates influenza survival, transmission, and seasonality. Proceedings of the National Academy of Sciences, 106(9), 3243-3248, DOI: 10.1073/pnas.0806852106, 2009.

Shao, X., Zhang, Y., Liu, C., Chiew, F. H., Tian, J., Ma, N., & Zhang, X.: Can indirect evaluation methods and their fusion products reduce uncertainty in actual evapotranspiration estimates?. Water Resources Research, 58(6), e2021WR031069, https://doi.org/10.1029/2021WR031069, 2022.

Smith, S. R., Hughes, P. J., & Bourassa, M. A.: A comparison of nine monthly air–sea flux products. International Journal of Climatology, 31(7), 1002-1027, https://doi.org/10.1002/joc.2225, 2011.

Sun, H., Chen, J., Yang, Y., Yan, D., Xue, J., Wang, J., & Zhang, W.: Assessment of long-term water stress for ecosystems across China using the maximum entropy production theory-based evapotranspiration product. Journal of Cleaner Production, 349, 131414, https://doi.org/10.1016/j.jclepro.2022.131414, 2022.

Sun, H., Sun, X., Chen, J., Deng, X., Yang, Y., Qin, H., ... & Zhang, W.: Different types of meteorological drought and their impact on agriculture in Central China. Journal of Hydrology, 627, 130423, https://doi.org/10.1016/j.jhydrol.2023.130423, 2023.

Sung, M. K., An, S. I., Shin, J., Park, J. H., Yang, Y. M., Kim, H. J., & Chang, M: Ocean fronts as decadal thermostats modulating continental warming hiatus. Nature communications, 14(1), 7777, https://doi.org/10.1038/s41467-023-43686-1, 2023.

Tang, R., Wang, Y., Jiang, Y., Liu, M., Peng, Z., Hu, Y., ... & Li, Z. L.: A review of global products of air-sea turbulent heat flux: accuracy, mean, variability, and trend. Earth-Science Reviews, 104662, https://doi.org/10.1016/j.earscirev.2023.104662, 2023.

Tian, W., Liu, X., Wang, K., Bai, P., Liu, C., & Liang, X.: Estimation of global reservoir evaporation losses. Journal of Hydrology, 607, 127524, https://doi.org/10.1016/j.jhydrol.2022.127524, 2022.

Tomita, H., Hihara, T., & Kubota, M.: Improved satellite estimation of near-surface humidity using vertical water vapor profile information. Geophysical Research Letters, 45(2), 899-906, https://doi.org/10.1002/2017GL076384, 2018.

Tomita, H., Hihara, T., Kako, S. I., Kubota, M., & Kutsuwada, K.: An introduction to J-OFURO3, a third-generation Japanese ocean flux data set using remote-sensing observations. Journal of Oceanography, 75(2), 171-194, https://doi.org/10.1007/s10872-018-0493-x, 2019.

Tomita, H., Kutsuwada, K., Kubota, M., & Hihara, T.: Advances in the estimation of global surface net heat flux based on satellite observation: J-OFURO3 V1. 1. Frontiers in Marine Science, 8, 612361, https://doi.org/10.3389/fmars.2021.612361, 2021.

Von Schuckmann, K., Minière, A., Gues, F., Cuesta-Valero, F. J., Kirchengast, G., Adusumilli, S., ... & Zemp, M.: Heat stored in the Earth system 1960–2020: where does the energy go?. Earth System Science Data, 15(4), 1675-1709, https://doi.org/10.5194/essd-15-1675-2023, 2023.

Wang, ~~F., Shen, Y., Chen, Q., & Wang, W.: Bridging the gap between GRACE and GRACE follow-on monthly gravity field solutions using improved multichannel singular spectrum analysis. Journal of Hydrology, 594, 125972, https://doi.org/10.1016/j.jhydrol.2021.125972, 2021.~~

~~Wang,~~ J., & Bras, R. L.: A model of evapotranspiration based on the theory of maximum entropy production. Water Resources Research, 47(3), https://doi.org/10.1029/2010WR009392, 2011.

Wang, J., & Bras, R. L.: An extremum solution of the Monin–Obukhov similarity equations. Journal of the atmospheric sciences, 67(2), 485-499, https://doi.org/10.1175/2009JAS3117.1, 2010.

Wang, J., Bras, R. L., Nieves, V., & Deng, Y.: A model of energy budgets over water, snow, and ice surfaces. Journal of Geophysical Research: Atmospheres, 119(10), 6034-6051, https://doi.org/10.1002/2013JD021150, 2014.

Wang, K., & Dickinson, R. E.: A review of global terrestrial evapotranspiration: Observation, modeling, climatology, and climatic variability. Reviews of Geophysics, 50(2), https://doi.org/10.1029/2011RG000373, 2012.

Wang, W., Chakraborty, T. C., Xiao, W., & Lee, X.: Ocean surface energy balance allows a constraint on the sensitivity of precipitation to global warming. Nature Communications, 12(1), 2115, https://doi.org/10.1038/s41467-021-22406-7, 2021.

Wentz, F. J., Ricciardulli, L., Hilburn, K., & Mears, C.: How much more rain will global warming bring?. Science, 317(5835), 233-235, DOI:10.1126/science.1140746, 2007.

Wielicki, B. A., Barkstrom, B. R., Harrison, E. F., Lee III, R. B., Smith, G. L., & Cooper, J. E.: Clouds and the Earth's Radiant Energy System (CERES): An earth observing system experiment. Bulletin of the American Meteorological Society, 77(5), 853-868, https://doi.org/10.1175/1520-0477(1996)077%3C0853:CATERE%3E2.0.CO;2, 1996.

Xu, T., Guo, Z., Xia, Y., Ferreira, V. G., Liu, S., Wang, K., ... & Zhao, C.: Evaluation of twelve evapotranspiration products from machine learning, remote sensing and land surface models over conterminous United States. Journal of Hydrology, 578, 124105, https://doi.org/10.1016/j.jhydrol.2019.124105, 2019.

Yang, Y., & Roderick, M. L.: Radiation, surface temperature and evaporation over wet surfaces. Quarterly Journal of the Royal Meteorological Society, 145(720), 1118–1129, https://doi.org/10.1002/qj.3481, 2019.

Yang, Y., Roderick, M. L., Guo, H., Miralles, D. G., Zhang, L., Fatichi, S., ... & Yang, D.: Evapotranspiration on a greening Earth. Nature Reviews Earth & Environment, 4(9), 626-641, https://doi.org/10.1038/s43017-023-00464-3, 2023.

Yang, Y., Sun, H., Zhu, M., Wang, J., & Zhang, W.: An R package of maximum entropy production model to estimate 41 years of global evapotranspiration. Journal of Hydrology, 614, 128639, https://doi.org/10.1016/j.jhydrol.2022.128639, 2022.

1174   Yin, Y., Wu, S., Chen, G., & Dai, E.: Attribution analyses of potential evapotranspiration changes in China
1175   since the 1960s. Theoretical and applied climatology, 101, 19-28, https://doi.org/10.1007/s00704-009-
1176   0197-7, 2010.

1177   Yu, L., X. Jin, and R. A. Weller.: Multidecade Global Flux Datasets from the Objectively Analyzed Air-sea
1178   Fluxes (OAFlux) Project: Latent and sensible heat fluxes, ocean evaporation, and related surface
1179   meteorological variables. Woods Hole Oceanograp, 2008.

1180   Yu, L.: A global relationship between the ocean water cycle and near-surface salinity. Journal of Geophysical
1181   Research: Oceans, 116(C10), https://doi.org/10.1029/2010JC006937, 2011.

1182   Zeng, X., Zhao, M., & Dickinson, R. E.: Intercomparison of bulk aerodynamic algorithms for the
1183   computation of sea surface fluxes using TOGA COARE and TAO data. Journal of Climate, 11(10),
1184   2628-2644, https://doi.org/10.1175/1520-0442(1998)011%3C2628:IOBAAF%3E2.0.CO;2, 1998.

1185   Zhao, G., & Gao, H.: Estimating reservoir evaporation losses for the United States: Fusing remote sensing
1186   and modeling approaches. Remote Sensing of Environment, 226, 109-124,
1187   https://doi.org/10.1016/j.rse.2019.03.015, 2019.

1188   Zhao, G., Gao, H., Naz, B. S., Kao, S. C., & Voisin, N.: Integrating a reservoir regulation scheme into a
1189   spatially distributed hydrological model. Advances in Water Resources, 98, 16-31,
1190   https://doi.org/10.1016/j.advwatres.2016.10.014, 2016.

1191   Zhao, G., Li, Y., Zhou, L., & Gao, H.: Evaporative water loss of 1.42 million global lakes. Nature
1192   Communications, 13(1), 3686, https://doi.org/10.1038/s41467-022-31125-6, 2022.